Final version published in Quaternary Geochronology available here:
https://www.sciencedirect.com/science/article/pii/S1871101420300133

The suitability of a low temperature post-IR IRSL signal for dating alluvial and colluvial "cut and fill" sequences in the Great Karoo, South Africa.

*C.J. Oldknow[a], A. S. Carr[b], J. M. Hooke[a], Z. Shen[c]

[a]*Department of Geography and Planning, Roxby Building, University of Liverpool, L69 7ZT.*

[b]*School of Geography, Geology, and the Environment, Bennett Building, University of Leicester, LE1 7RH.*

[c]*Department of Marine Science, Coastal Carolina University, USA.*

**Corresponding author; Email: cjo61@liv.ac.uk*

Abstract

Alluvial and colluvial "cut and fill" deposits preserved in valleys of the Karoo, South Africa, reflect basin-scale adjustments in fluvial process-regime. Such deposits in the Wilgerbosch catchment have previously proven difficult to date using radiocarbon (^{14}C) and optically stimulated luminescence (OSL) methods. In this paper, we test the suitability of K-feldspar post-IR infrared (pIRIR) methods on 19 samples from Africanders Kloof, a low-order tributary of the Sundays River. Using three carefully screened quartz OSL ages, radiocarbon dating and site stratigraphic considerations we argue that the $pIRIR_{170}$ protocol can be used to produce reliable age estimates. Fading rates for the $pIRIR_{170}$ signal are consistently low (average g_{2days}: 0.81 ± 0.58). The $pIRIR_{170}$ residuals are dose dependent (r^2=0.58); but are consistently low as a proportion (e.g. 1-4%) of sample equivalent dose (D_e). Despite the water-lain depositional context, single aliquot D_e distributions tend toward normality (for 11/19 samples) irrespective of aliquot size (2 mm or micro-aliquots containing 2-30 grains) with only a few statistical outliers per sample (max. n=3) and overdispersion (OD) ranging from 1.6-30% excluding the two youngest (late Holocene) samples (OD: 37-87%). The resulting $pIRIR_{170}$ ages are in the correct stratigraphic order and illustrate the potential of $pIRIR_{170}$ luminescence dating to investigate the timing, processes and drivers of fluvial system adjustments across the Karoo.

Keywords: K-rich feldspar; Post-IR IRSL; OSL; Bleaching; Fading.

1. Introduction

Alluvial and colluvial sediments in tectonically stable settings like the South African Karoo constitute important archives of fluvial/slope system adjustments (Botha and Fedoroff, 1995; Marker, 1995; Holmes et al., 2003; Grenfell et al., 2014; Oldknow and Hooke, 2017) and, in some cases, late Quaternary climate change (Clarke et al., 2003; Lyons et al., 2014). Early applications of luminescence methods in such contexts included infrared stimulated luminescence (IRSL) and thermoluminescence (TL) dating of colluvial deposits of the Masotcheni formation on the Great Escarpment (Botha et al., 1994; Botha and Fedoroff, 1995; Wintle et al., 1993). These showed much promise based on good agreement with independent radiocarbon age control (e.g. Wintle et al., 1995a; 1995b). More recently, optically stimulated luminescence (OSL) dating of quartz has proven to be a reliable dosimeter for alluvial and colluvial deposition in the eastern Karoo (Rodnight, 2006; Keen-Zebert et al., 2013; Lyons et al., 2013), but the upper age limit is constrained at some sites by high environmental dose rates (Clarke et al., 2003; Temme et al., 2008).

In contrast, Oldknow and Hooke (2017) sought to apply OSL dating to a complex alluvial and colluvial stratigraphy in the Wilgerbosch catchment, Sneeuberg (Fig. 1), but met with limited success. This was due variously to low quartz yields, a dim OSL signal, feldspar contamination, and/or OSL saturation (i.e. at less than 40 ka) caused by relatively high environmental dose rates (> 4 Gy ka^{-1}). Therefore, an alternative luminescence chronometer needs to be considered.

The suitability of K-feldspar post-IR IRSL (pIRIR) methods in relation to water-lain deposits has yet to be investigated in this part of the Karoo. This approach utilizes a slower or non-faded signal obtained via a second higher temperature IRSL signal administered after a lower temperature IRSL measurement (typically at 50^{o}C and denoted as IRSL$_{50}$; Thomsen et al., 2008; Buylaert et al., 2009; 2012). Despite the increased stability of the pIRIR signal relative to previously used IRSL$_{50}$ protocols, a number of studies have shown it bleaches more slowly than the IRSL$_{50}$ and quartz OSL signals (e.g. Godfrey-Smith et al., 1988; Buylaert et al., 2012; 2013; Kars et al., 2014; Colarossi et al., 2018; Riediesel et al., 2018). This is of particular concern for sediments deposited in water-lain contexts (e.g. glacio-fluvial, fluvial, lacustrine) where equal sunlight bleaching of all grains cannot be guaranteed (Sohbati et al., 2012; Trauerstein et al., 2014; Smedley et al., 2015; Braumann et al., 2018; Carr et al., 2019). Yet, some studies from such environments have shown that even for late Holocene deposits, the pIRIR signals (e.g. $pIRIR_{170}$ and $pIRIR_{225}$) are sufficiently bleached and single aliquot results show excellent agreement with independent dating control (e.g. Ainscoe et al., 2019, Buckland et al., 2019; Smedley et al., 2019).

The basic compromise when selecting pIRIR stimulation temperatures is that while lower temperature post-IR stimulation (e.g. at 150 or 170^{o}C as opposed to 225 or 290^{o}C) may result in enhanced bleachability, lower residuals and therefore reduced risk of age over-estimation (e.g. Madsen et al., 2011; Lowick et al., 2012; Reimann et al., 2011; 2012; Kars et al., 2014; Colarossi et al., 2015); the risk of higher anomalous fading rates increases (Jain et al., 2015), potentially necessitating fading corrections (Huntley and Lamothe, 2001; Huntley, 2006).

Additionally, age overestimation may not always result from poor bleaching. For example the size of the test dose employed during pIRIR measurements has been shown to result in dose recovery overestimation (e.g. for test doses <15% of D_e, Yi et al., 2016; Colarossi et al., 2018). Working on alluvial samples from the Moopetsi River, South Africa, Colarossi et al. (2015) generated $pIRIR_{225}$ ages that overestimated (>100%) independent age (quartz OSL) control for samples older than 20 ka due to use of an unsuitably small test dose. However, the residuals in their study were not excessively high (11 ± 1.3 Gy) considering the chosen stimulation temperature and depositional context. Nevertheless, dating of young deposits (i.e. < 20 ka) in this and similar alluvial contexts may benefit from the use of a lower temperature pIRIR signal to minimize the size of the residual pIRIR as much as possible.

The aim of this paper is therefore to establish whether it is possible to identify and utilize a sufficiently bleached, non- or low-fading pIRIR signal capable of decoding the age structure of a complex alluvial/colluvial cut and fill sequence in the Wilgerbosch catchment. If successful, this would represent a significant breakthrough in demonstrating the potential of pIRIR to investigate fluvial landscape evolution possibly up to glacial-interglacial timescales in the wider Karoo region.

2. Study area

The Great Karoo is a vast (30% land surface of South Africa) dissected landscape of plains and flat-topped mountains, characterized by east-west orientated mountain ranges such as the Sneeuberg (Fig. 1A). The Sneeuberg lies within the eastern region of the warm temperate zone at a major climatic junction between summer- and winter-dominated rains (Sugden, 1989; Chase and Meadows, 2007). Average annual rainfall is about ~423 mm and is concentrated in the late summer/early autumn (Grenfell et al., 2014). Diurnal and seasonal temperatures show large fluctuations: summer maxima of ca. 30 ^{o}C in summer and winter minima of below -10 ^{o}C (Schultz, 1980). The Wilgerbosch catchment includes several low-order tributaries (Fig. 1B) which comprise the headwaters of the Sundays River (Fig. 1A). Africanders Kloof within Wilgerbosch is a mixed alluvial-bedrock stream incised into slopes of Balfour Formation (part of the Triassic-age Beaufort Group) sandstones and mudstones (Turner, 1978). These sedimentary rocks represent deposition in braided river and lacustrine settings. Plagioclase (e.g. anorthoclase) is more abundant than K-feldspars in these rocks (oligoclase, andesine and some microcline). Quartz occurs as mono- and polycrystalline varieties, the former tending to contain inclusions (Oghenekome, 2012). These sedimentary rocks are hypothesized to have been derived from eroding metamorphosized felsic volcanic rocks such as granitic gneisses (Bhatia, 1983).

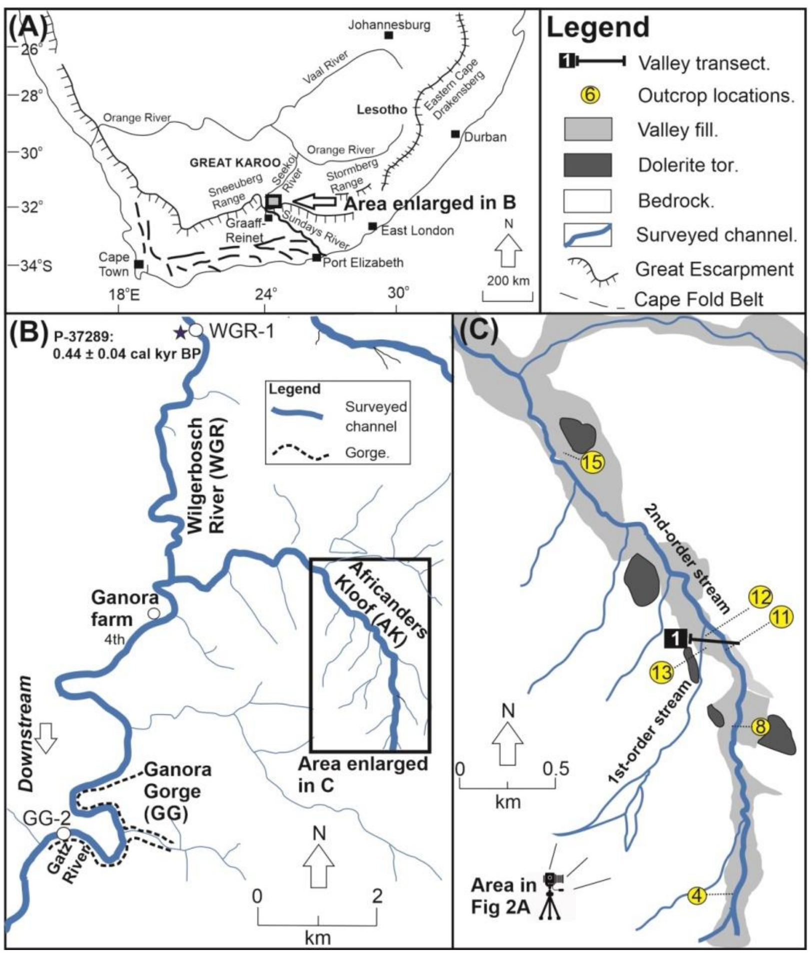

Fig. 1. (A) Map of Republic of South Africa highlighting the study area; (B) map of the Wilgerbosch catchment digitized from aerial photographs; (C) map of the low-order tributary "Africanders Kloof" showing locations of transects and outcrops selected for pIRIR dating, dolerite tors and surveyed limits of valley fills.

Note: (i) the blue star at the top of the system denotes a radiocarbon age from outcrop WGR-1 (P-37289, see Fig. 3); (ii) outcrop GG-2 referred to throughout the text (see Fig. 9, Oldknow and Hooke, 2017).

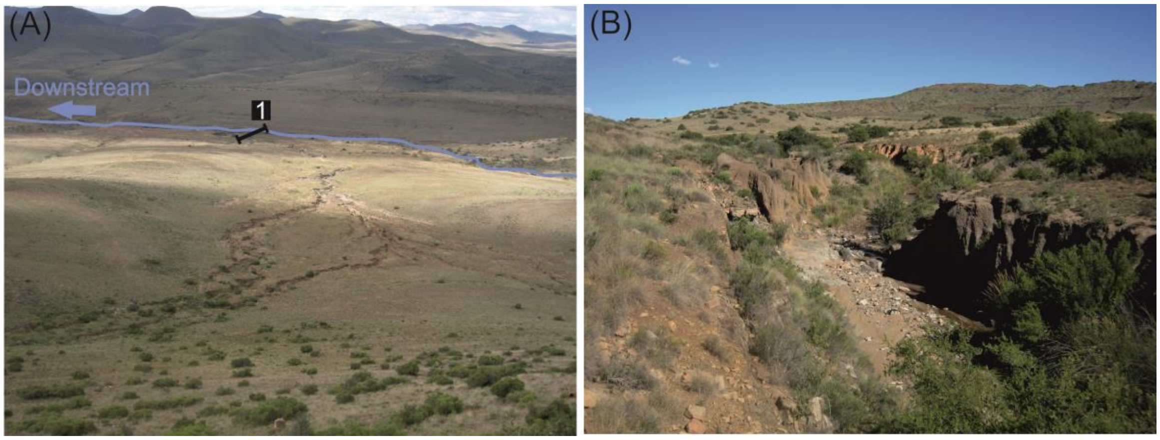

Fig. 2. Africanders Kloof: (A) Photograph of the catchment looking northeast taken from headwaters at location shown in Fig. 2B, highlighted is transect 1; (B) Photograph of valley fills at transect 1, looking upstream.

These sedimentary strata are intruded by resistant Drakensberg Group dolerite sills and dikes. The dolerites are subalkaline tholeiitic basalts comprised of Ca-rich plagioclases (labradorite, bytownite, anorthite (in phenocrysts)), pyroxene, olivine, magnetite and skeletal ilmenite (Cox et al., 1967; Ramluckan, 1992; Neumann et al., 2011). Quartz is present only as an accessory mineral.

The vegetation of the study area is characterized by 'Eastern Upper Nama-Karoo (NKu2)' on gently sloping hills and is dominated by dwarf shrubs and grasses of the genera *Aristida* and *Eragrostis*. Thin soils, stones and boulders on steeper sandstone slopes and dolerite ridges support dwarf Karoo shrubs and drought tolerant grasses (*Aristada, Eragrostis,* and *Stipagrostis*) of the 'Upper Karoo Hardeveld (NKu4)' (Mucina et al., 2006).

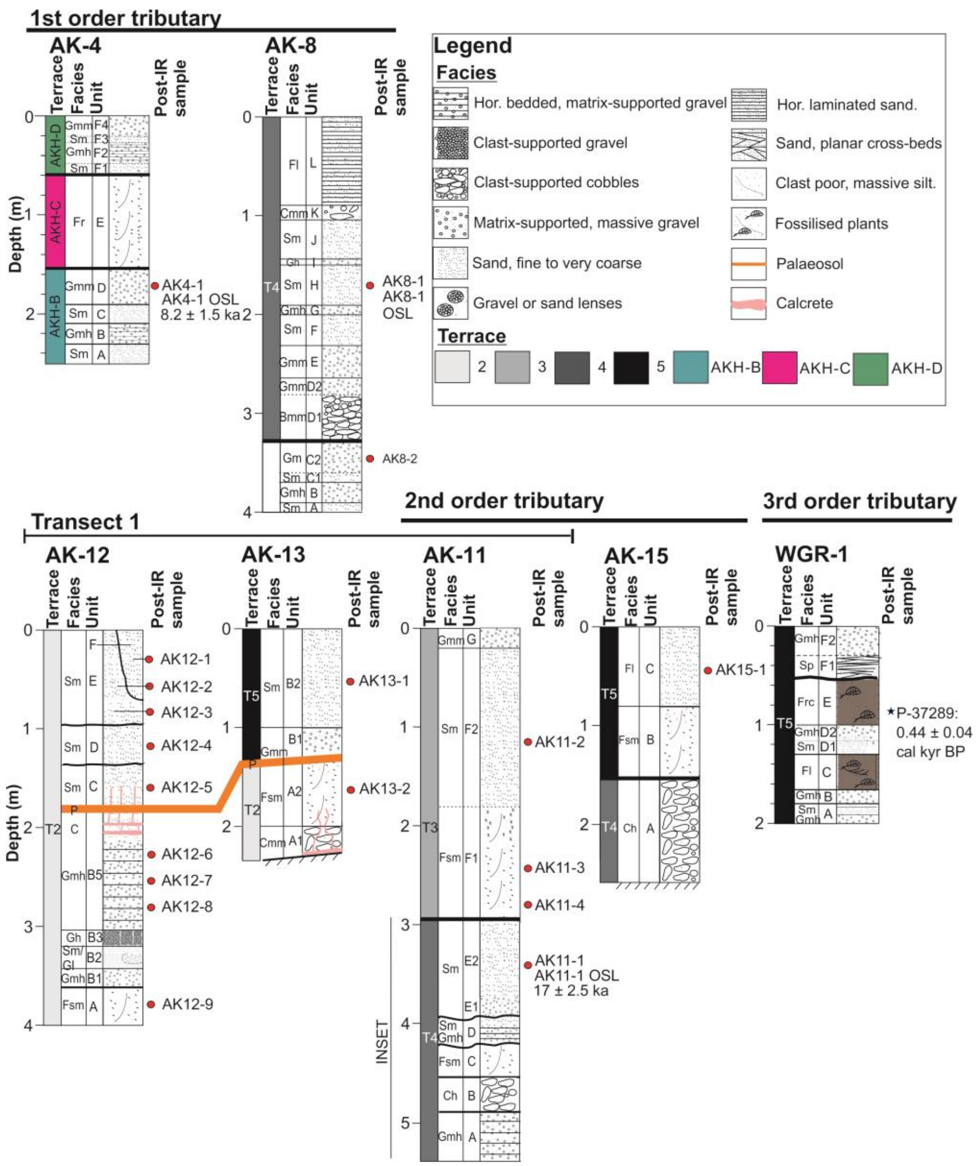

Fig. 3. Summary of the sedimentary succession at outcrops exposed in Wilgerbosch (see Fig 1, for outcrop locations). Indicated are the locations of: (i) samples taken for pIRIR dating; (ii) existing quartz OSL ages (AK4-1, AK11-1); and (iii) a repurposed quartz OSL sample dated in this study (AK8-1). Note: radiocarbon age (0.44 ± 0.04 cal kyr BP) referred to throughout the text. Facies codes are modified from Miall (1996). Grain size terminology follows the Udden-Wentworth (1922) scale. Some of the stratigraphic relations between these fills have been revised (from Oldknow and Hooke, 2017) in light of subsequent field observations. OSL prefix codes have been changed from LV- (as reported in Oldknow and Hooke, 2017) to AK- in this study for consistency.

The basin is infilled by at least four extensive terrace fills in the higher order tributaries which have been interpreted as evidence of basin-wide cyclic cut and fill (Oldknow and Hooke, 2017). The low-order tributaries and upper slopes contain thick (6 m) colluvial deposits which are overlain by discontinuous flood-out deposits (outcrop AK-4, Fig. 1C and 3. Oldknow and Hooke (2017) obtained an OSL age (8.2 ± 1.5 ka) from a flood-out at outcrop AK-4 (see Figs. 1C and 3). The alluvial succession and locations of pIRIR samples are provided in Fig. 3. The sampling scheme ensured complete representation of the stratigraphy with a view to developing a chronology of cut and fill at the specified sites. The sedimentology and stratigraphy of deposits and locations of new luminescence dating samples are described as follows.

T1 comprises diamictic deposits up to 6 m thick in the Ganora Gorge. Vertically orientated, matrix-supported gravel-sized sandstone clasts attest to local slope- rather than alluvial sedimentation. Oldknow and Hooke (2017) hypothesized these deposits accumulated due to colluvial activity during the Last Glacial Maximum.

T2 (outcrops AK12 and AK13) is characterized by two facies associations: 1) units composed of silty sand (unit A) and matrix-supported horizontally-bedded gravels (unit B) which display upward fining to sand (top of unit B); and 2) sandy silt units (units C–E) with evidence of disturbance by modern root channels within 1 m of the surface. These two facies groups are interpreted as channel deposits and overbank sediments respectively. An infilled palaeogully (unit F) is unconformably carved into unit E. A distinct rubified palaeosol horizon punctuates the succession (separating units B and C) and is indicative of a prolonged phase of geomorphic stasis. Vertical calcified root channels originating in unit C time-transgress this palaeosol unconformity intersecting with a calcrete horizon up to 10 cm thick, overprinting unit B. Micromorphological analyses have revealed that this calcrete is “rhizogenic” (Wright, 1990; Oldknow, 2016) and formed in association with a phreatic root system accessing an elevated water table (Wright et al., 2005).

T3 is only partially exposed at outcrop AK11 due to an inset deposit up to 2.4 m thick (T4). T3 consists of thick units of inversely graded silty sand (unit F1) and sandy silt (unit F2); buried by matrix-supported gravels (unit G). Oldknow and Hooke (2017) interpreted these facies as indicative of slopewash rather than channel or overbank sedimentation.

In contrast, T4 at profile AK11 is characterized by normally-graded, horizontally-bedded units including matrix-supported gravels (units A and D), clast-supported cobbles (unit B), silty sands (unit C); and a relatively thick (~1 m) homogeneous sand unit (unit E) from which a quartz OSL age (AK11-1: 17 ± 2.5 ka) was obtained (Oldknow and Hooke, 2017). These deposits are interpreted as a migrating single-thread channel. In particular, the elevation and thickness of high-energy palaeo-flood deposits (unit B) corresponds to debris flow facies (e.g. AK8 unit D) in close proximity to an eroding dolerite tor (see Fig. 1C). On this basis, Oldknow and Hooke (2017) proposed that the aggradation recorded at T4 (AK11; this study) must have resulted from a phase of strong slope-channel connectivity

(AK-8), implying that both the OSL and pIRIR ages for samples AK8-1 and AK11-1 ages should be concordant with one another.

T5 is characterized by well-sorted sandy silt (e.g. AK13 unit B2) or organic-rich silty sands containing plant macrofossils (e.g. AK15 unit B). It is interspersed with coarser gravel and sand units with inverse grading in the Wilgerbosch River. These facies indicate valley-floor wetland systems with low-energy channels that later incised due to land-use changes introduced during the European incursion (Boardman, 2014). An AMS ^{14}C age (P-37289; 0.44 ± 0.04 cal kyr BP, outcrop WGR-1, Fig. 2) was obtained from fossilized *Juncus* stems and provides a maximum age for the incision of these wetlands (Oldknow and Hooke, 2017). Rowntree (2013) and Boardman (2014) demonstrated gully erosion in this area was active at the start of the 20th century. Therefore, new pIRIR ages from AK13-1 and AK15-1 should bracket or overlap with this radiocarbon age.

Where possible samples for dating were obtained from relatively well-sorted homogeneous units of sandy silt or silty sand (13 of 19 samples). These are indicative of deposition in the lower-flow regime, either as slopewash (e.g. AK11-3), single-thread channels (e.g. AK11-1) or channel overbank (e.g. AK12-4) contexts.

Incomplete bleaching is most likely to be a challenge for samples collected from coarser (higher energy) channel deposits coupled with the shortest transportation distances (e.g. AK8-1). Samples collected from units previously subjected to waterlogging (e.g. AK12-6 to AK12-9; AK13-1) may also have been affected by variability in water content and external environmental dose. Indeed, a further advantage of using pIRIR methods in this context is the partial mitigation of these factors via the dose rate contribution from internal K and Rb.

3. Methods

The three ages previously reported (two quartz OSL, one ^{14}C) from the Wilgerbosch sequence offer a key benchmark against which to test pIRIR age reliability, especially the potential issue of bleaching. However, given the problems with quartz OSL in this area (Boardman et al., 2005; Oldknow, 2016), additional screening of the published OSL ages (samples AK4-1 and AK11-1, originally LV-509 and LV-515 in Oldknow and Hooke, 2017) as well as analysis of a new OSL sample (AK8-1) was undertaken to more thoroughly investigate the purity of the quartz. K-feldspar was then extracted from the same samples, dated with a low temperature pIRIR protocol and compared to the quartz OSL results.

3.1. OSL analyses

Preparation methods for OSL samples AK4-1 and AK11-1 were carried out at the University of Liverpool in 2015 and reported in detail in Oldknow (2016). In summary, 90-300 and 90-200 µm grains for AK4-1 and AK11-1 (respectively) were obtained via wet sieving. 10% v/v HCl and 30% v/v H_2O_2 were used to remove carbonates and organic matter. Density separation using sodium polytungstate provided the quartz fraction (2.62 < ρ <2.76 g/cm^2). High feldspar contents (>50%) necessitated use of the large grain size windows and a strong (40% v/v for 40 mins) HF etch to remove feldspar from the quartz fraction (Mauz and Lang, 2004). OSL analyses were conducted on a Risø DA-15 B/C reader equipped with 21 blue LEDs (470Δ30 nm; 80% of full diode current providing ~17 mW cm^{-2}). Measurements were carried out using the SAR protocol (Murray and Wintle, 2000) employing blue (125 ^{o}C) stimulation with luminescence detected through a Hoya U340 filter (transmitting 320-390 nm). The routine IR-depletion test to detect feldspar contamination was included (Duller, 2003). Data analysis was undertaken in Analyst v.4.31 (Duller, 2015). Dose response curves (DRC herein) were fitted using a single saturating exponential function to obtain the best fit (reduced χ^2 parameter). D_e values were determined by integrating the initial 0.48s of the decay curves and subtracting the signal from a late background (10s).

Aliquots were rejected based on: (i) low OSL count rates (<300); (ii) recycling ratio >10% from unity; (iii) detection of feldspar contamination (IRSL depletion ratio >10% from unity; Duller, 2003); (iv) failure to fit an exponential function to growth curve; and (v) recuperation >5%. SAR protocol suitability was tested using combined preheat/dose recovery tests. Oldknow (2016) found that dose recovery performance for AK4-1 was poor due to recuperation (Aitken and Smith, 1988) when using the standard SAR protocol. A dose recovery experiment was thus setup to test a variant of the SAR protocol which incorporated a high temperature OSL stimulation (in addition to the standard blue 125 ^{o}C stimulation) into the T_x part of the SAR cycle. For this dose recovery test, OSL stimulation temperature was varied from 200-280 ^{o}C (duration 40 s). An OSL stimulation temperature of 220 ^{o}C (for 40 s) coupled with a preheat of 200 ^{o}C and cutheat of

180 ^{o}C, was found to yield lowest recuperation values (e.g. <2%); and was employed to obtain 46 equivalent dose (D_e herein) estimates on 1 mm aliquots. For sample AK11-1, the standard SAR protocol (Murray and Wintle, 2000; Duller, 2003) was employed using a preheat of 240 ^{o}C and cutheat of 200 ^{o}C to obtain 61 D_e estimates on 1 mm aliquots (Oldknow, 2016).

Sample AK8-1 was prepared and measured at the University of Leicester using a Risø DA20 TL/OSL reader equipped with 28 blue LEDs (470Δ30 nm; 70% of full diode current providing ~70 mW cm^{-2}), with quartz luminescence detected through a Hoya U340 filter and IRSL through Schott BG39 and Corning 7-59 filters (also used to measure K-feldspar ages, section 3.2). This sample produced a relatively large quartz yield compared to AK4-1 and AK11-1, permitting use of a narrower grain size window (90-125 µm). A combined preheat/dose recovery test was used to verify the suitability of the SAR protocol (administered dose 43.6 Gy). A preheat of 220 ^{o}C and a cutheat of 200 ^{o}C (Fig. S1) resulted in best dose recovery (average 1.03 ± 0.02 n=12). SAR protocol measurements (following Table S2a) produced 43 D_e estimates on 1 mm aliquots. Data analyses and integration limits used were the same as specified previously.

For all three OSL samples, few (<5%) aliquots exhibited IRSL indicative of ‘feldspar’ contamination; but certain kinds of K-rich feldspar (e.g. sanidine), Ca-rich (e.g. labradorite) and Na-rich (e.g. anorthoclase) plagioclases do not emit UV under IR excitation (Duller and Bøtter-Jensen, 1993; Mauz and Lang, 2004).

As such types of non-UV emitting feldspar are potentially present given the geological context at Wilgerbosch (section 2.1), a series of alternative non-standard luminescence tests to screen for feldspar contamination were carried out. 1) Thermal quenching (cf. Wintle, 1975). A pure quartz sample exhibits "thermal quenching" with increased stimulation temperature (Duller et al., 1995) while feldspar exhibits "thermal assistance" (McKeever et al., 1997). A modified SAR protocol whereby the stimulation temperature was varied (from 50-325 ^{o}C at 20 ^{o}C intervals) was applied to 8 aliquots of each sample (Table S3). The resultant OSL versus stimulation temperature curves (Fig. S2) were fitted with the thermal quenching formula of McKeever et al. (1997) using the OriginPRO9 function fitter:

(1) $I = I_0 / (1 + C \exp(-W / kT))$

Where W is the thermal activation energy, I is the OSL intensity, I_0 is the initial OSL intensity, k is the Boltzmann constant and C is a constant. Pure quartz should exhibit a W value of around 0.51 eV (Wintle, 1975; Shen et al., 2007) with W values ~0.2 eV reported for feldspar (Poolton et al., 2002; Shen et al., 2007).

2) The ratio of IR intensity to TL intensity at 110 ^{o}C (IR/TL herein) employed by Li et al. (2002). Most feldspars exhibit TL at 110 ^{o}C, but unlike quartz do not exhibit a single peak; rather they manifest as the rising limb (thermal assistance) of higher temperature TL peaks (McKeever et al., 1997). As only some feldspars emit UV under IR stimulation, but most feldspars exhibit thermal assistance (post 110 ^{O}C), the IR/TL ratio is more sensitive to polymineral mixtures than the IR-

depletion test alone (Duller, 2003). Mauz and Lang (2004) demonstrated that IR/TL ratios approaching 0 are indicative of pure quartz, while IR/TL ratios closer to 1 indicate feldspar contamination. They cautioned however that as the IR/TL ratio only considers signal intensity at a specific temperature (110 ^{o}C), interpretation of the IR/TL ratio should be coupled with qualitative appraisal of the shape of the TL peak. Thus, we define two additional aliquot rejection criteria: 1) Aliquots which demonstrate thermal assistance (rather than thermal quenching) above 110^{o}C; and/or 2) IR/TL values >0.25. In such instances, a QUANTAX micro-XRF (X-ray fluorescence) unit fitted to a Hitachi TM4000 benchtop scanning-electron microscope (SEM) was used to diagnose the nature of the contamination in both morphological and geochemical terms.

3.2. Post-IR IRSL methods

K-feldspar grains were extracted by treating each of the 19 samples with 10 % v/v HCl and 32 % v/v of H_2O_2 to remove carbonates and organics, respectively. Wet sieving isolated the coarsest fraction possible (controlled by sample amount) and was usually 180- or 212-250 µm (Table S1). Density separation utilizing sodium polytungstate provided the 2.53-2.58 g cm^{-3} K-rich feldspar fractions, which were then etched in 10% HF for 10 minutes. 2 mm aliquots (several hundred grains) and micro-aliquots (2-30 grains) were analysed using a pIRIR protocol comprising a low temperature (50 ^{o}C) initial stimulation, followed by a high temperature (pIRIR) stimulation (Table S2b). IRSL for the 50 ^{o}C was measured for 100 s; IRSL for the high temperature stimulation was measured for

300 s. Samples were preheated for 60 s at a temperature set 30 ^{o}C above pIRIR stimulation temperature following Roberts (2012).

The choice of pIRIR stimulation temperature (150, 170, 225 and 290 ^{o}C) was then based on degree of overlap between the pIRIR ages (AK4-1, AK8-1, AK11-1, AK15-1) with independent age control (section 3.1; 4.1). The signal that exhibited the strongest overlap was then subjected to further analyses and ultimately applied to the remaining 15 samples. A bleaching test was conducted (following Buckland et al., 2019) to assess the magnitude of the residual IR_{50} and pIRIR signals after different time intervals (i.e. 0, 10, 30, 60 minutes and 4 days) of exposure to direct (UK) sunlight (section 4.2).

Sensitivity of the chosen pIRIR signal to test dose size (13-60% of D_e) was undertaken (section 4.3), while anomalous fading rates (section 4.4) were determined following Auclair et al. (2003) with g-values and corrections (following Huntley and Lamothe, 2001) determined using the R package “Luminescence” (Kreutzer et al., 2012).

Dose recovery tests (herein DRTs) and additional residual dose measurements were performed to assess the robustness of the SAR protocol (section 4.5). Bleaching was achieved by exposing samples to natural UK daylight for 48 hours. The administered beta dose was matched to the sample D_e and measured using the protocol outlined in Table S2b. Additionally, an “added dose” approach to dose recovery was used (Buylaert et al., 2011) which does not rely on complete bleaching of the sample prior to analysis.

Data analysis was undertaken in Analyst v.4.31 (Duller, 2015). Dose response curves were fitted using a single saturating exponential function to obtain the best fit (reduced χ^2 parameter). D_e values were determined by integrating the initial 10s of the decay curves and subtracting the signal from a late background (30s). For all IRSL measurements, aliquots were only accepted if: (i) recycling ratio was ± 10% of unity; (ii) recuperation was <5% of the natural dose; (iii) the error on the test dose signal was less than 3 standard deviations of the background signal; (iv) the uncertainty on the test dose luminescence measurement was less than 10%. Recuperation as a percentage of the natural signal was high for the very young sample AK15-1 (expected age between 0.1-0.5 ka~) and aliquots exceeding 5% recuperation were still included in order to avoid potential overestimation of burial dose (D_b) (e.g. Buckland et al., 2019).

The resulting D_e distributions, utilizing all accepted aliquots are presented using Abanico plots (Dietze et al., 2016; Fig. 10, S7). Identification and removal of D_e outliers (both OSL and pIRIR) was based on values lying outside 1.5 x the interquartile range (IQR) (Medialdea et al., 2014). After removal, D_e values were averaged using the central age model (CAM) (Galbraith et al., 1999). Two samples (AK12-9 and AK13-2) were used to investigate in more detail the sensitivity of D_e to aliquot size (section 4.6) via a comparison of ages obtained from micro-aliquot and 2 mm aliquot measurements.

3.3. Dose rate determination

Element concentrations were determined via inductively coupled plasma mass spectrometry (ICP-MS) for U and Th and ICP-OES for K, at the University of Leicester. U, Th and K concentrations were converted to annual dose rates following Guerin et al. (2011) with corrections for grain size (Mejdahl, 1979), water content (Aitken, 1985) and HF etching (Bell, 1979). For K-feldspar, the internal K and Rb dose rates assume grain K and Rb concentrations of 12.5 ± 0.5% and 400 ± 100 ppm respectively (Huntley and Baril, 1997; Huntley and Hancock, 2001). Cosmic dose rates were determined using the profile elevation (metres above sea-level, herein masl) and the measured sample depth (Prescott and Hutton, 1994) with a 5% relative uncertainty.

Final age uncertainties incorporate 3% relative uncertainties for each of the dose rate conversion factors, grain size attenuation and HF etching, propagated via standard methods. HF etching is assumed to have entirely removed the α-irradiated outer portion of the grains. The ICP-MS derived external beta dose rates were validated by comparison with beta dose rates obtained via GM beta counting. These show good correspondence (Fig. S3).

Taking the calcrete as a surrogate of the maximum upper limit of the palaeowater-table (section 2), an average burial water content of 15 ± 5% (Oldknow and Hooke, 2017) was used in age calculations for any samples below it (AK12-6 to AK12-9). For samples above the calcrete, the measured water content was used. A 5% change in water content results in a ~2000 year age difference for samples aged ~50 ka and ~1200 years for samples aged ~30 ka.

4. Results

4.1. Quartz OSL verification tests and OSL ages

Table 1 indicates that thermal activation values (*W*) for each of the quartz samples are consistent with published values for pure quartz (e.g. 0.51 eV, Shen et al., 2007). Two aliquots of AK4-1 were 'atypical' (*W* = 0.36 eV) but still higher than published values for feldspar (e.g. 0.19 eV, Shen et al., 2007).

The TL curves for each sample possess 110 ^{o}C peaks that are typical of quartz (Fig. S4a). Exceptions include three aliquots of AK4-1 (Fig. S4b - red line). Sample AK11-1 is notably more problematic as a stable background post-110 ^{o}C is not reached for >75% of aliquots and for 9 aliquots, the TL observed at 110 ^{o}C does not occur as a single peak; but as a thermally assisted rising limb of a higher temperature peak indicative of feldspar (Fig. S4b). Six of these nine aliquots also exhibit IR/TL values >0.25 that are consistently higher than AK4-1 and AK8-1 (Table 1) and correspond to IR/TL values indicative of feldspar contamination (Li et al., 2002; Mauz and Lang, 2004). When D_e is plotted as a function of IR/TL for these aliquots (Fig. S5), a weak inverse (-0.28, $p<0.05$) correlation is observed, which, in conjunction with the shape of the TL curve, indicates a 'faded' feldspar luminescence signal.

SEM analyses of etched quartz grains (AK11-1) adjudicates the question of the contamination registered by the luminescence-based tests. Observations include Na and Mg-rich opaque and translucent grains in conjunction with “glassy” transparent Si-rich (quartz) grains (Fig. S6) indicating either inclusions within the quartz or feldspar grains. On this basis, the aforementioned nine aliquots of AK11-1 were rejected and the sample age recalculated in comparison to the published age.

Table 1

Range and mean values of selected OSL-based parameters (thermal activation energy *W*; IR/TL ratio) to assess quartz purity.

Sample	*W* range	*W* mean	IR/TL range	IR/TL mean
AK4-1	0.36-0.7	0.56	0.02-0.24	0.07
AK8-1	0.41-0.66	0.50	0.04-0.27	0.12
AK11-1	0.45-0.57	0.49	0.05-0.65	0.20

To summarize, samples AK4-1 and AK8-1 exhibit quartz OSL characteristics that justify their use as a benchmark against which to test pIRIR protocol performance and pIRIR signal bleaching. AK11-1 is contaminated, but the clear TL 110 ^{o}C peak exhibited by 52/61 aliquots attests to the overall dominance (in luminescence terms) of suitable quartz.

Table 2

Results of quartz OSL analyses and revised ages.

[a]Number of aliquots used in final age calculation.

[b]Overdispersion parameter.

[c] Central Age Model D_e.

* Recalculated D_e and OD values after outlier removal (Fig. S7).

Sample	n[a]	σ_{OD} (%)[b]	D_e (Gy)[c]	Final age (ka) (1 σ)
AK4-1	43	32	33.8 ± 1.7	8.0 ± 1.3
AK8-1	43 *40	21 *17	38.4 ± 2.0 *37.0 ± 1.1	15.6 ± 0.8 *15.0 ± 0.8
AK11-1	52 *45	24 *16	55.8 ± 1.9 *53.4 ± 1.3	15.4 ± 2.6 *14.7 ± 2.6

The OD for the AK8-1 D_e is quite high (21%) considering both the grain size (90-125 µm) and aliquot size of this sample, but is moderately skewed (0.99) by three high outliers (>60 Gy). Removal of these outliers and recalculation of the central age model (CAM) D_e moves the age from 15.6 ± 0.8 ka to 15.0 ± 0.8 ka and lowers the OD to 17% (Table 2; Fig. S7). Seven statistical outliers were identified for AK11-1 (Fig. S7). Their removal moves the CAM age from 15.4 ± 2.6 ka to 14.7 ± 2.6 ka and lowers the OD to 16% (Table 2).

4.2. pIRIR signal selection

The suitability of different elevated temperature post-IR stimulations (i.e. $pIRIR_{150, 170, 225, 290}$) was assessed by comparing the results for K-rich feldspar fractions extracted from samples AK4-1, AK8-1 and AK11-1 with their corresponding quartz OSL age control (Table 2, Fig. 4).

Figure 4 shows that the $pIRIR_{150}$ ages underestimate the OSL ages, while the $pIRIR_{225}$ and $pIRIR_{290}$ tend to overestimate the OSL ages. $pIRIR_{290}$ age AK8-1 significantly overestimates (~50%) the OSL age. In contrast, the $pIRIR_{170}$ and OSL ages for all three samples show consistent overlap.

Figure 5 shows the $pIRIR_{170}$ luminescence behaviour and D_e distributions. Results are expanded to include $pIRIR_{170}$ data from a fourth sample (AK15-1) which comes from a stratigraphic horizon coeval with radiocarbon age P-37289 (section 2). Despite the larger D_e of samples AK8-1 and AK11-1 (up to 63.6 ± 1.2 Gy) compared to AK15-1 and AK4-1 (up to 41.1 ± 1.2 Gy), the IRSL signals are not especially bright (max. ~7000 counts). This could be a consequence of less "potassic" K-feldspar variants (e.g. sanidine) within the sediments at Wilgerbosch (section 3).

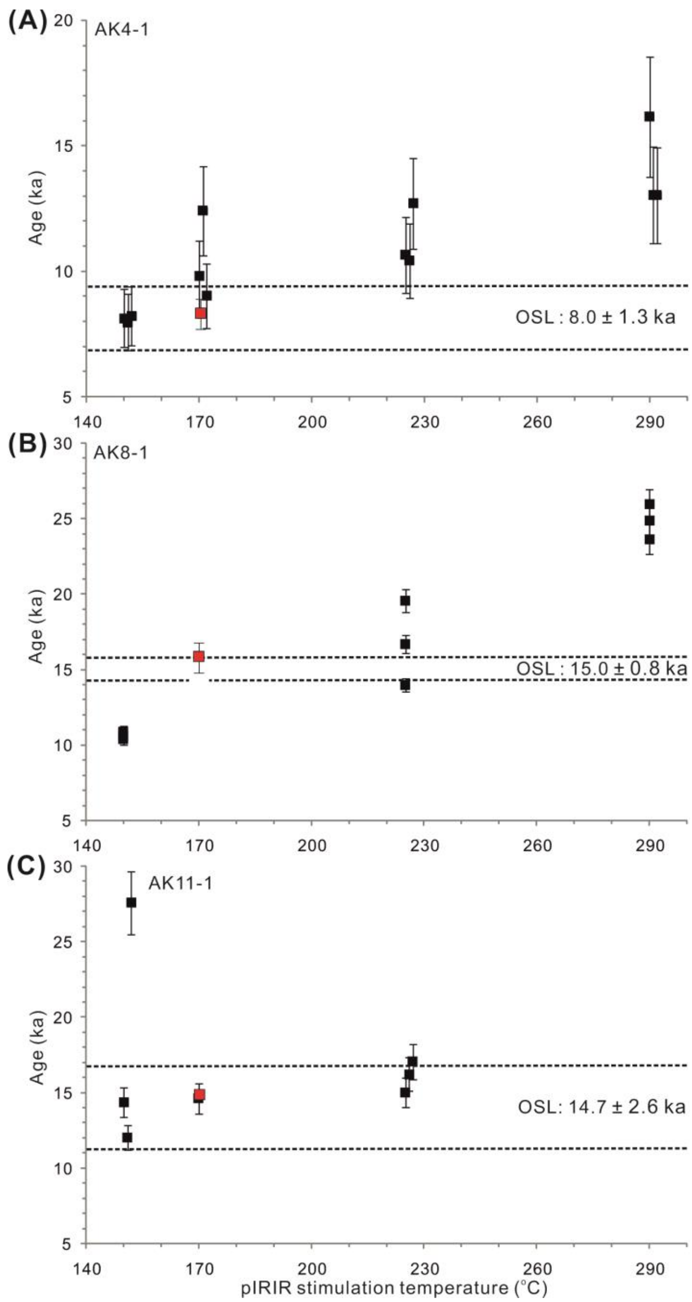

Fig. 4. Fading-uncorrected pIRIR ages (ka) obtained from 2 mm aliquot measurements for different pIRIR stimulation temperatures. Note: (i) red squares denotes CAM pIRIR$_{170}$ ages (based on 12, 13 and 14 aliquots respectively) which overlap the quartz ages (1σ error); (ii) 3 aliquots at the other stimulation temperatures were measured; (iii) the pIRIR$_{290}$ was not measured for AK11-1 based on its tendency to overestimation.

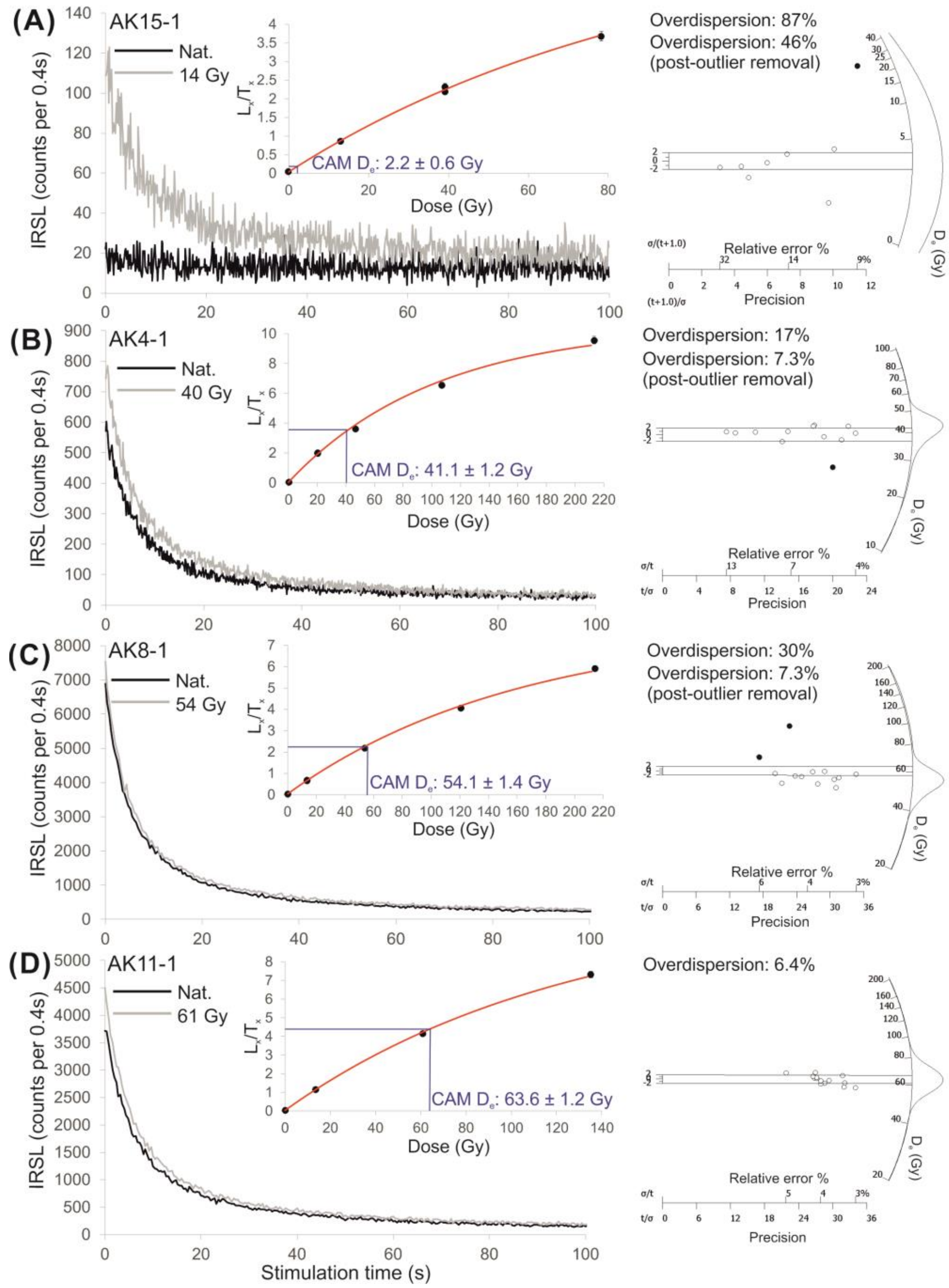

Fig. 5. Shine-down curves, dose response curves (fitted using a single saturated exponential function) and radial plots for the $pIRIR_{170}$ measurements on (A) AK4-1, (B) AK8-1, (C) AK11-1 and (D) AK15-1. Samples are ranked from youngest (AK15-1) to oldest (AK11-1). Outlier D_e values are marked in black. Note: AK15-1 D_e data are based on micro-aliquot measurements; the other samples were measured using 2 mm aliquots.

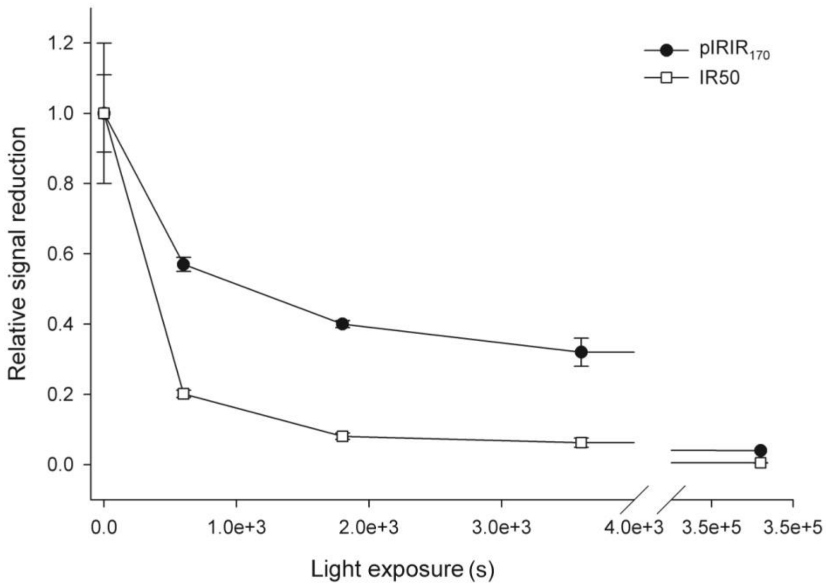

Fig. 6. Results of bleaching experiment in direct UK sunlight using a sample (AK12-8) with a large D_e ($pIRIR_{170}$: 222 Gy; IR_{50}: 133 Gy). Residual IR_{50} and $pIRIR_{170}$ signal measured after 0, 10, 30, 60 minutes and 4 days (3.5e+5 secs).

The D_e distributions presented in Fig. 5 range from normal (AK4-1, AK11-1) to positively skewed due to 1-2 high outlier aliquots (see also Table S6: AK8-1, AK15-1). AK15-1 is overdispersed (87%), but exhibits a small D_e (2.2 ± 0.6 Gy). Despite a single high outlier for AK15-1 (29.2 Gy), its CAM $pIRIR_{170}$ age (0.6 ± 0.3 ka) is in good agreement with ^{14}C age P-37289 (0.44 ± 0.04 cal kyr BP).

Sample AK4-1 exhibits an OD of 17%. Removal of a single low outlier (19 Gy) reduces OD (7.3%) and moves the CAM $pIRIR_{170}$ age from 8.2 ± 0.5 ka to 8.6 ± 0.3 ka (Table 4). AK8-1 is rather more dispersed (OD: 30%) considering its (2 mm) aliquot size, but removal of two high outliers (89 and 151 Gy) brings its $pIRIR_{170}$ age from 18 ± 1.5 ka to 16.1 ± 0.4 ka, which is in better agreement (1 σ error) with the OSL age (Figure 4, Tables 2 and 4). Sample AK11-1 exhibits very low OD (6.4%).

Figure 6 demonstrates that more than one hour of sunlight exposure is required to reduce the $pIRIR_{170}$ signal of sample AK12-8 to less than 33% of its original intensity (from a dose of 222 Gy). In contrast the IR_{50} signal intensity is reduced by ~90% (of 133 Gy) after 30 minutes ($1.8x10^3$ seconds). After 4 days of light exposure, the $pIRIR_{170}$ signal was reduced to 4% (8.9 Gy) and the IR_{50} to 1% (1.3 Gy) of their original signals. This equates to residual ages of 2.1 ka and 0.3 ka respectively (dose rate 4.21 Gy/ka, Table S1). This $pIRIR_{170}$ residual age is four times greater than that of AK15-1 (Table 4) and 25% the magnitude of age AK8-1; yet both of these ages are concordant with independent age control. This is considered further in section 4.5.

In summary, as the $pIRIR_{170}$ signal produces ages in strong agreement with independent age control and bleaches quickly, a pIRIR protocol comprising a 50 ^{o}C IRSL stimulation followed by a subsequent 170 ^{o}C stimulation was used (Table S2b) in subsequent experiments, and to determine K-feldspar luminescence ages.

4.3. Test dose size

Figure 7 shows little variation in sample age is observed with changing test dose size (13-60% of D_e), although precision tends to be higher (see AK4-1 and AK11-2) for moderate test doses (22-32%). Thus, a ~30% test dose was applied to all SAR measurements (Table S2b).

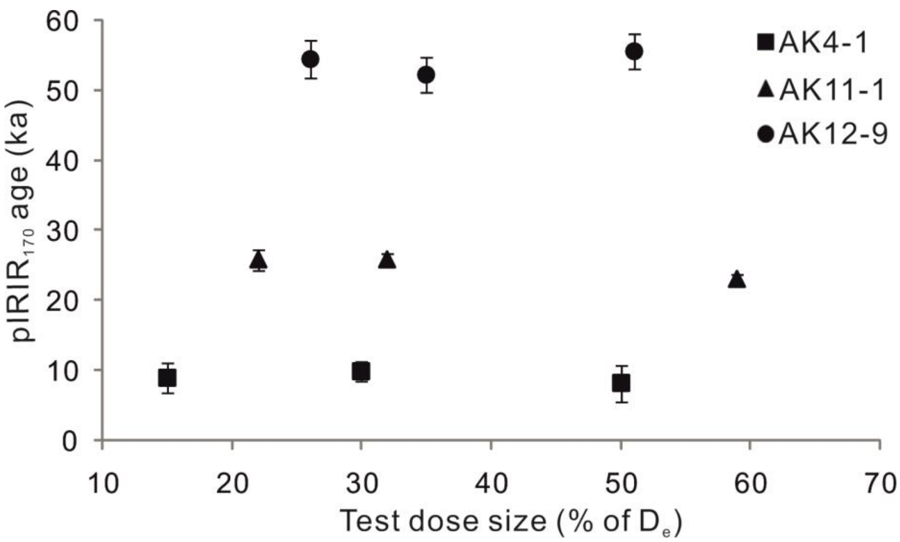

Fig. 7. Impact of test dose size (% of D_e) on $pIRIR_{170}$ ages.

4.4. Anomalous fading

Tables 3 and S4 show fading rates (g_{2days}) for 17 of the 19 $pIRIR_{170}$ and IR_{50} samples respectively. The $pIRIR_{170}$ fading rates are 0.29 ± 1.06%, 0.75 ± 0.54% and 0.15 ± 0.36% for samples AK4-1, AK8-1 and AK11-1 respectively. Consistently low g-values were obtained for all samples (average g_{2days} value 0.81 ± 0.58%, max 1.76% per decade, WGK4-1) removing the need for fading correction (Huntley and Lamothe, 2001). The IR_{50} fading rates are non-trivial (average 2.58 ± 0.6%). Fading is 2.48 ± 0.52%, 2.15 ± 0.59% and 4.95 ± 0.51% per decade for samples AK4-1, AK8-1 and AK11-1 respectively. Fading correction brings the IR_{50} ages into strong (e.g. AK4-1) and better (e.g. AK8-1, AK11-1) agreement with both the $pIRIR_{170}$ and OSL ages (Fig. 8, Tables 2 and S5).

The effectiveness of the fading correction method (e.g. Huntley and Lamothe, 2001), however, is contingent upon sample D_e residing on the linear part of the DRC. As illustrated in Fig. 5, the D_e of the older samples (e.g. AK11-1) lies on the exponential part of the DRC which may account for the tendency of the IR_{50} ages to underestimate the $pIRIR_{170}$ ages above ~15-20 ka (Fig. 8A). For the oldest sample (e.g. AK8-2), the underestimation of the fading-uncorrected IR_{50} is >50% (Fig. 8B).

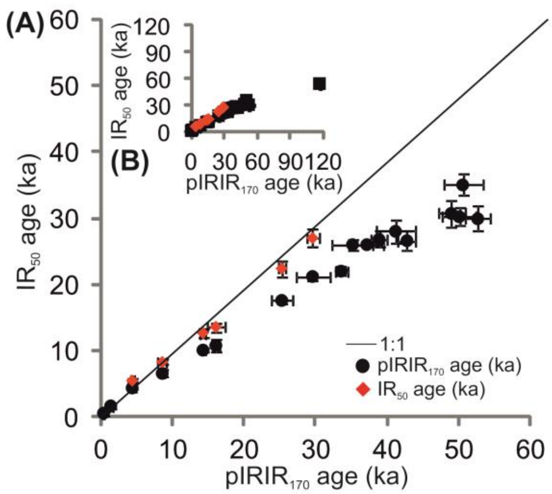

Fig. 8. (A) Comparison of IR_{50} ages before and after fading correction (Huntley and Lamothe, 2001) with $pIRIR_{170}$ ages. Highlighted are samples constrained by independent age control (Fig. 5); (B) Inset includes the oldest sample (AK8-2, see Table 4). Note tendency for fading-corrected IR_{50} ages to slightly underestimate the $pIRIR_{170}$ ages >15 ka.

4.5. Suitability of the $pIRIR_{170}$ SAR protocol

Tables 3 and S4 summarize results of residual dose and dose recovery experiments for the $pIRIR_{170}$ and IR_{50} signals respectively. Tables 4 and S5 summarize $pIRIR_{170}$ and IR_{50} D_e and ages respectively. Aliquot acceptance using standard SAR criteria was consistently high (> 80%) irrespective of aliquot size (2 mm aliquots or micro-aliquot).

Table 3.

Internal checks of $pIRIR_{170}$ protocol performance carried out on 2 mm aliquots. Note: (i) dose recovery ratios (DRR) are average values using all measured (n=3) aliquots; (ii) AK8-2 and AK12-X were subjected to two DRTs using low and high administered doses; (iii) AK12-X was used during preliminary testing and not dated.

Sample	DRR Natural Light	DRR Added dose	g_{2days} (% per decade)	Residual dose (Gy).
AK4-1	-	-	0.29 ± 1.06	-
AK8-1	0.99 ± 0.04	-	0.75 ± 0.54	2.30 ± 0.16
AK8-2	-	1.01 ± 0.02 (66.9 Gy) 0.89 ± 0.04 (401.5 Gy)	0.10 ± 0.47	6.23 ± 1.19
AK11-1	-	-	0.15 ± 0.36	-
AK11-2	0.96 ± 0.01 *1.12 ± 0.03	-	0.99 ± 0.50	3.00 ± 0.5
AK11-3	1.09 ± 0.04	-	0.68 ± 0.56	3.88 ± 0.83 *6.95 ± 0.91
AK11-4	-	-	-	-
AK12-1	0.97 ± 0.02	-	1.61 ± 0.38	-
AK12-2	1.04 ± 0.04	0.97 ± 0.03	0.89 ± 0.71	-
AK12-3	-	0.95 ± 0.03	0.85 ± 0.49	5.72 ± 0.15 *9.40 ± 1.4
AK12-4	-	0.88 ± 0.02	0.79 ± 0.65	-
AK12-5	0.93 ± 0	-	0.62 ± 0.44	4.00 ± 0.7
AK12-6	-	-	0.73 ± 0.62	-
AK12-7	-	0.95 ± 0.05	1.22 ± 0.74	6.31 ± 1.09 *11.33 ± 1.13
AK12-8	1.14 ± 0.02	1.03 ± 0.01	0.98 ± 0.61	20.60 ± 2.2
AK12-9	-	-	0.01 ± 0.57	-
WGK4-1	0.96 ± 0.01	-	1.76 ± 0.71 *0.83 ± 0.43	4.20 ± 0.3 *8.80 ± 3.3
AK12-X	-	1.04 ± 0.01 (65.4 Gy) 0.94 ± 0.01 (366.3 Gy)	0.53 ± 0.49	-
Average	**1.01 ± 0.01**	**0.95 ± 0.05**	**0.81 ± 0.58**	**6.30 ± 0.64** ***9.12 ± 0.71**

*Refers to $pIRIR_{225}$ measurements given for comparative purposes.

The $pIRIR_{170}$ residual doses are dose-dependent (Li et al., 2013) and range from 1-4% of sample D_e except AK12-8, the residual dose of which is ~9% (Fig. S10). The DRR of sample AK12-8 after bleaching in natural light overestimated (1.14 ± 0.02) the given dose (220 Gy); but the added dose experiment yielded a DRR close to unity (1.03 ± 0.01). Sample AK12-7 from the same stratigraphic unit exhibited a much smaller residual dose (6.31 ± 1.09 Gy; ~3% of D_e) and good dose recovery (added dose DRR: 0.95 ± 0.05), yet its D_e overlaps with AK12-8

(Table 4). Since the D_e of sample AK12-8 does not appear to incorporate a large residual (~9% of D_e or 20 Gy) relative to sample AK12-7 (from the same stratigraphic unit), we propose that the dose recovery overestimation for the former reflects inadequate bleaching conditions under natural daylight (Buckland et al., 2019). Excluding AK12-8, the sample with the largest residual is thus AK8-1, which is 4% of its D_e or 0.7 ka. Subtraction of this residual makes no difference to the $pIRIR_{170}$ age. which overlaps with the faster-bleaching quartz OSL age (Fig. 4). The residuals were therefore not subtracted from sample D_e values in this study (following Li et al., 2013).

Of the 12/19 samples measured for dose recovery, 9 exhibited good $pIRIR_{170}$ dose recovery performance. Sample AK8-2 has the highest D_e (501 Gy) and although it is not saturated, a high administered beta dose (402 Gy) resulted in dose recovery underestimation (0.89 ± 0.04). A smaller administered dose (67 Gy) yielded a DRR at unity (1.01 ± 0.02). A similar underestimation was observed for a comparatively young (e.g. AK12-4) sample (0.88 ± 0.02) whose age was consistent with other samples (e.g. AK12-3 and AK13-2) from the same stratigraphic unit that showed good dose recovery (Table 3).

4.6. $pIRIR_{170}$ D_e distributions

Figure 9 compares micro-aliquot and 2 mm aliquot $pIRIR_{170}$ D_e values for two samples. The degree of inter-aliquot scatter in $pIRIR_{170}$ D_e values increases down to the micro-aliquot (i.e. <5 grain) level, but the average D_e essentially remains the same. As a result, the CAM D_e (even if 3-4 grains are measured, see

AK13-2) is comparable with the 2 mm aliquot CAM D_e data. In addition, Table 4 shows that the ages determined using different aliquot sizes for these two samples overlap within 1σ. The same is true of the bracketing ages, irrespective of aliquot size.

Table 4.

Results of pIRIR$_{170}$ D_e measurements for 2 mm aliquots (top) and micro-aliquots (bottom). Shown on the left are the number of aliquots measured over the number passing the rejection criteria (n/n), the observed OD, the CAM D_e and resulting CAM ages. Shown on the right are the number of statistical outliers removed (N) and the resulting final OD, CAM D_e and CAM ages (ka). Note: Samples dated using both 2 mm and micro-aliquots (AK12-9 and AK13-2) are emboldened for comparison. They overlap within 1σ implying insensitivity of D_e to aliquot size.

2mm aliquots								
All accepted aliquots					Post-outlier removal			
Sample	n/n	OD%	CAM D_e (Gy)	Age (ka)	N	OD%	CAM D_e (Gy)	Age (ka)
AK4-1	12/13	17	39.2 ± 2.1	8.2 ± 0.5	1	7.3	41.1 ± 1.2	8.6 ± 0.3
AK8-1	13/14	30	60.7 ± 5.1	18.0 ± 1.5	2	7.8	54.1 ± 1.4	16.1 ± 0.4
AK8-2	7/7	11	501.1 ± 24.0	121.3 ± 5.8	1	9.3	485.0 ± 22.0	117.4 ± 5.3
AK11-1	14/15	6.4	63.6 ± 1.2	14.3 ± 0.3	-	-	-	-
AK11-2	18/18	4.9	122.5 ± 1.8	25.3 ± 1.4	2	1.2	122.4 ± 1.2	25.3 ± 1.4
AK11-3	13/13	7.5	127.0 ± 3.0	29.6 ± 2.4	-	-	-	-
AK12-1	12/12	4.0	14.5 ± 0.4	4.4 ± 0.4	-	-	-	-
AK12-5	18/18	4.8	184.8 ± 3.2	37.2 ± 2.2	-	-	-	-
AK12-8	13/16	1.6	221.8 ± 11.0	52.7 ± 1.8	-	-	-	-
AK12-9	**7/7**	**9.6**	**208.0 ± 10.5**	**51.4 ± 2.6**	**1**	**1**	**217.4 ± 2.4**	**53.7 ± 2.6**
AK13-2	**12/12**	**6.2**	**178.8 ± 3.8**	**41.9 ± 3.8**	**1**	**3.5**	**175.9 ± 2.8**	**41.2 ± 2.8**

Micro-aliquots								
All accepted aliquots					Post-outlier removal			
Sample	n/n	OD%	CAM D_e (Gy)	Age (ka)	N	OD%	CAM D_e (Gy)	Age (ka)
AK11-4	18/22	29	126.9 ± 8.7	30.8 ± 2.1	2	9.7	138.3 ± 3.8	33.6 ± 0.9
AK12-2	24/24	28	165.3 ± 9.6	39.0 ± 2.3	3	14	164.4 ± 5.6	38.9 ± 1.2
AK12-3	18/18	21	186.9 ± 9.8	42.3 ± 2.2	2	9.3	189.2 ± 5.3	42.8 ± 1.2
AK12-4	14/18	22	167.0 ± 10	37.5 ± 2.2	2	15	156.7 ± 7.4	35.2 ± 2.9
AK12-6	13/13	21	238.0 ± 15	53.7 ± 3.4	2	17	224.0 ± 12	50.6 ± 2.7
AK12-7	10/13	14	224.0 ± 12	49.0 ± 2.6	2	6.9	224.1 ± 8.1	49.0 ± 1.9
AK12-9	**17/18**	**18**	**202.8 ± 9.4**	**50.1 ± 2.3**	**-**	**-**	**-**	**-**
AK13-1	13/17	37	6.9 ± 0.7	1.6 ± 0.2	2	14	6.0 ± 0.3	1.4 ± 0.2
AK13-2	**13/16**	**29**	**162.0 ± 14**	**37.9 ± 3.3**	**2**	**11**	**167.5 ± 7.4**	**39.2 ± 1.7**
AK15-1	8/14	87	3.2 ± 1.3	0.6 ± 0.3	1	46	2.2 ± 0.6	0.4 ± 0.1

The results of 2 mm aliquot and micro-aliquot D_e determinations are presented in Table 4 and Fig. S9. Skewness and kurtosis in relation to OD are presented in Table S6. In general, and as expected, 2 mm aliquot D_es are less dispersed (OD: 1.6-30%, average 6.4%) compared to the micro-aliquot D_es (OD: 14-87%, average 26%). The pIRIR$_{170}$ OD values are comparable with those from the IR$_{50}$ D_e distributions, but are higher for four samples (AK11-4, AK12-2, AK12-4 and AK13-2, see Tables 4 and S5). CAM D_es range from 3-501 Gy, tend to be fairly normally distributed (skewness <1 for 11/19 samples) and possess only a few outliers (max. 3 per sample). The impact of these outliers on the pIRIR$_{170}$ CAM ages is small. They usually consist of 1-2 high outlier aliquots (e.g. AK12-2; AK15-1), but are sometimes counterbalanced by a low outlier of similar magnitude (e.g. AK12-2) or in a few cases a very low (i.e. > 3 x IQR) outlier (e.g. AK11-4). AK11-4 is negatively skewed (-1.67) and dispersed (29%) due to two such low outliers, which after removal lowers the OD (9.7%) and moves the CAM age from 30.8 ± 2.1 to 33.6 ± 0.9 ka. Notably, the resultant CAM ages for all samples are in correct stratigraphic order and consistent with stratigraphy (Figures 3 and 10).

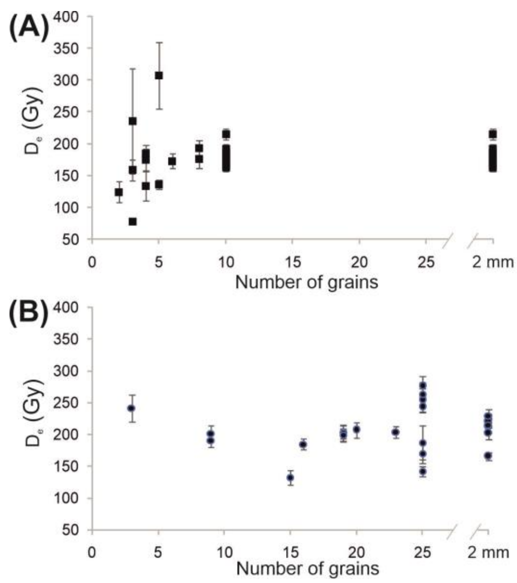

Fig. 9. Equivalent doses (D_e) plotted as a function the number of grains per aliquot for samples AK13-2 (A) and AK12-9 (B). Note: Two sets of ages for AK13-2 and AK12-9 are reported in Table 4 based on micro-aliquot (2-25 grains) and 2 mm aliquots.

5. Discussion

5.1. Overall performance of the pIRIR$_{170}$ protocol

The strong overlap between the pIRIR$_{170}$, quartz OSL (Fig. 4), fading-corrected IR$_{50}$ ages (Fig. 8) and ^{14}C age P-37285 (section 4.2) indicates that the necessary pre-condition for bleaching (for the pIRIR$_{170}$) of around or less than ~2 days sunlight exposure (section 4.5) has been most completely achieved for facies deposited under subcritical flow conditions.

For facies deposited under high-energy flow conditions coupled with having been eroded from a nearby source (sample AK8-1), there is a slight overestimation of the pIRIR$_{170}$ age compared to the OSL age, but this is substantially less pronounced than for ages obtained using higher temperature post-IR stimulations (pIRIR$_{225,}$ pIRIR$_{290}$). The pIRIR$_{290}$, which bleaches the most slowly (Smedley et al., 2019), appears unsuitable in this catchment (Fig. 4). While the pIRIR$_{225}$ demonstrated reasonable overlap with independent age control (e.g. AK4-1, AK11-1), table 3 shows that the residuals are still higher on average (7% of D$_e$) than the pIRIR$_{170,}$ similar to published values (11 ± 1.3 Gy, cf. Colarossi et al., 2015). Coupled with the fact the pIRIR$_{170}$ is non-faded, the pIRIR$_{170}$ is preferable in this catchment. The pIRIR$_{225}$ could potentially be utilized for dating older deposits (e.g. sample AK8-2: >100 ka) where the pIRIR$_{170}$ may underestimate D$_b$.

Furthermore, if during successive phases of valley filling sediments with a low rather than high D$_b$ were reworked, this would have also helped mitigate against the potential limitations for sunlight bleaching imposed by short transport distances and flow hydraulics. As bleaching appears to be non-limiting for the youngest samples (<15 ka), it follows that the relative impact of any partially-bleached grains was proportionally smaller for the majority of the $pIRIR_{170}$ ages which are older than 25 ka.

We now consider the performance of the $pIRIR_{170}$ protocol on the basis of internal checks (Table 3). In general, the high aliquot acceptance rate and good dose recovery indicates the $pIRIR_{170}$ SAR protocol is suitable for determining the D_b of these alluvial samples. The reason for DRR underestimation for AK8-2 is however unclear. This could be due to inadequate characterization of the DRC of this sample, considering its very high D_e. However, the fact that a comparable given dose of 366 Gy can be successfully recovered for another sample (e.g. AK12-X) implies that the $pIRIR_{170}$ protocol may be suitable for dating sediments in these valleys up to at least ~85-90 ka old.

The DRR overestimation in concert with the high residual dose measured for sample AK12-8 is most likely explicable in terms of varied bleaching conditions under natural daylight (e.g. Buckland et al., 2019). Were its large residual (20.6 ± 2.2 Gy – 9% of D_e) representative of a unusually large unbleachable signal for this sample, we would expect to see an excursion in the sample age relative to the bracketing ages, which is not the case.

5.2. Impact of aliquot size on $pIRIR_{170}$ D_e

The fact that the IR_{50} and $pIRIR_{170}$ D_e values exhibit relatively few statistical outliers is a further indication that partial bleaching is non-limiting in this instance (Trauerstein et al., 2014). The observation that micro-aliquots (Fig. 9) exhibit clear signals (> 3 sigma above background) implies that signal averaging may equally not be serious, but a full single grain analysis would be required to assess the degree of grain-to-grain signal variation (Rhodes, 2015). What is clear is that the distribution of micro-aliquot D_e values does not appear to differ greatly to that of the 2 mm aliquot D_e analyses. This - coupled with the further observations that there is strong agreement between: (i) $pIRIR_{170}$ ages based on 2 mm aliquot measurements and independent age control (section 4.1); and (ii) ages irrespective of aliquot size within the same stratigraphic unit (e.g. section AK12) - suggests that 2 mm aliquot CAM D_e values provide a reliable estimate of D_b. That the sample D_es appear to be reproducible using relatively few grains may attest to the higher efficiency of K-feldspar relative to quartz grains in representing the total population of D_e values within a given sample (Smedley et al., 2019).

5.3. Sources of scatter in $pIRIR_{170}$ D_e distributions

OD is aliquot-size dependent, increasing at the micro-aliquot scale (Fig. S9). Sample AK8-1 is the only example of a 2 mm aliquot $pIRIR_{170}$ age exhibiting high OD (~30%) most likely due to inclusion of partially bleached grains (section 5.1). Indeed, although several high D_e outliers were observed for other samples (e.g. AK12-2 to AK12-6, AK15-1), the associated OD (except the youngest samples) was always lower than AK8-1 even when micro-aliquots were used (e.g. AK13-2: OD 29%). Ages from profile AK12 overlap, irrespective of the presence of such outliers.

Final version published in Quaternary Geochronology available here:
https://www.sciencedirect.com/science/article/pii/S1871101420300133

The second possible extrinsic contributor to OD is bioturbation (Jankowski et al., 2014). Post-depositional mixing may be responsible for the low D_e outliers observed for samples AK4-1, AK11-4, AK12-2 to AK12-4 (Table 4; Fig. S9), as these sediments are friable, with physical evidence of disturbance by modern root channels in places. Intrusion of sand grains is not deemed likely immediately above and below the calcrete, based on micromorphological evidence which shows illuviation of just clay and silt grains Oldknow (2016).

The observation that D_e scatter increases down to the micro-aliquot scale (i.e. <10 grains, e.g. AK13-1) may indicate that sample OD is incorporating the effects of intrinsic factors (i.e. variations in K content, fading and microdosimetry), but an analysis of single grains would be required to assess their relative contributions (Rhodes, 2015).

In summary, sample OD tends to largely reflect few individual outliers, the presence of which makes minimal difference to the resulting CAM $pIRIR_{170}$ ages. Application of the outlier removal procedure (section 3.2) reduced OD to well below 20% except for the youngest sample (Table 4).

5.4. $pIRIR_{170}$ chronology of “cut and fill” and its implications

The final $pIRIR_{170}$ ages are presented in Fig. 10 and all are consistent with their stratigraphic positions. The samples collected from AK12 (T2) indicate two alluvial aggradational episodes at 51 ± 2 ka and 39 ± 2 ka (averages) punctuated by a phase of geomorphic stasis reflected in the palaeosol horizon. Taking the difference between these averages, this stasis must have been sustained over a period of at least 8 ka. Rhizogenic calcrete formation commenced around 39 ± 2 ka. These ages also indicate that the deposits comprising T1 (section 2.1) which were originally hypothesized to be LGM (Oldknow and Hooke, 2017), must in fact be older than 50 ka, possibly deposited during Marine Isotope Stage (MIS) 4.

The samples from T3 indicate a comparatively ‘slow’ phase of colluviation, with 2 m of deposition from 33.6 ± 0.9 to 25.3 ± 1.4 ka (ages AK11-4 to AK11-2). Given the age of the lowest sample (AK11-4), it is possible that the onset of aggradation coincided with floodplain sedimentation on T2 (AK12). This would imply that T2 in the first-order tributary did not incise, possibly as a result of the armouring effect of the calcrete (Oldknow and Hooke, 2017).

The two samples collected from T4 are indicative of alluvial channel aggradation at 16.1 ± 0.4 ka (AK8-1) and 14.3 ± 0.3 ka (AK11-1) in late MIS2. Although there are currently no bracketing samples from either profile, these ages are in close agreement (2σ) and consistent with morpho-stratigraphic correlations (Oldknow and Hooke, 2017).

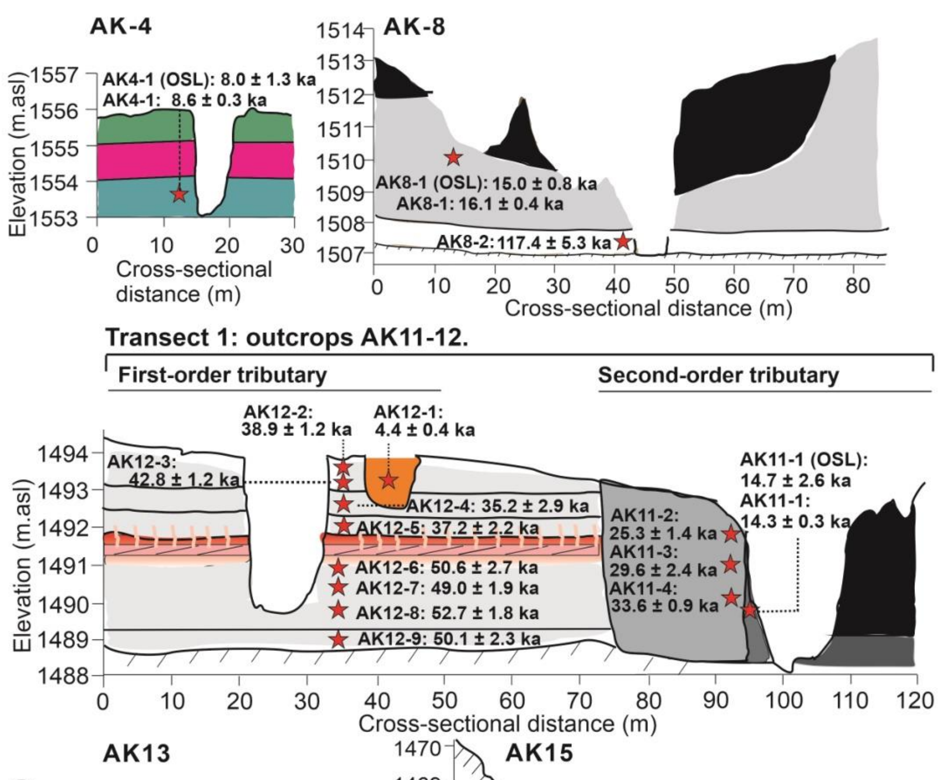

Fig. 10. Chronostratigraphy of the alluvial/colluvial succession comprising 3 quartz OSL and 19 new $pIRIR_{170}$ ages (see Tables 2 and 4). Note: 1) ages reported omit statistical outliers as outlined in the text; 2) all luminescence ages are $pIRIR_{170}$ except those labeled 'OSL'; and 3) see Fig 1C for locations of outcrops/transects.

A notable feature of the new chronostratigraphy is the lack of an early-mid Holocene record. The small palaeogully incised into T2 is the only deposit to yield a mid-Holocene age (AK12-1: 4.4 ± 0.4 ka). The samples collected from the fine-grained vlei (wetland) deposits (T5) date to 1.4 ± 0.2ka (AK13-1) and 0.4 ± 0.1 ka (AK15-1), consistent with the morphostratigraphic model of Oldknow and Hooke (2017) (their T4). These are at least 50% younger than the youngest vleis (2.5 ± 0.05 ka cal BP) reported in the nearby Klein Seekoi River (Holmes et al., 2003).

The chronology therefore indicates three phases of aggradation (~51, ~39, and ~33-25 ka) and an incision phase (~37-34 ka) in MIS3 where channel cutting exceeded terrace thickness. A key control on whether aggradation occurs is the degree of connectivity between thick weathering mantles on dolerite tors and/or colluvial deposits at various locations (e.g. GG-2, Fig. 1B) with the channel network. There may be connectivity when either (i) the valley floors are not buffered from the slopes by terrace deposits or (ii) there is gully headcutting into the slopes triggering a “sediment slug” (Oldknow and Hooke, 2017).

The potential role for climate in driving such episodes of connectivity has, until now, been untestable at Wilgerbosch. It is intriguing that the timing of palaeosol (48-41 ka) and wetland (~39 ka) development corresponds to dry (~46-41 ka) and relatively wet periods (41-28 ka) in the South African interior (Lyons et al., 2014). Colluviation in this period has been reported by Temme et al. (2008) in the Okhombe valley, and by Rowell et al. (2018) in the Stormberg Range (~35.2 ± 2.6 ka - 29.8 ± 3.1 ka), overlapping with the Wilgerbosch record (~33-25 ka, T3). The absence of MIS2 and MIS1 deposits at Wilgerbosch is the subject of ongoing investigation. Elsewhere in South Africa, the LGM was characterized by reduced (Keen-Zebert et al., 2013) or no sediment accumulation (Temme et al., 2008; Rowell et al., 2018), perhaps due to aridity (Lyons et al., 2014). However, Oldknow and Hooke (2017) suggested that the cementation of the oldest deposits (i.e. T1-T2) coupled with limited storage space at Africanders Kloof, could have led to disproportionate representation of the early part of the terrace record at the expense of younger fills. This may account for the limited expression of late MIS2 (e.g. AK8-1, AK11-1) and Holocene (e.g. AK13-1, AK15-

1) deposits in contrast to other nearby sites (e.g. Bousmann et al., 1988; Sugden, 1989; Marker, 1995; Holmes et al., 2003).

6. Conclusions

Nineteen samples from alluvial and colluvial cut and fill sediments were dated via the application of 2 mm aliquot and micro-aliquot $pIRIR_{170}$ measurements. Non-standard luminescence based tests to screen for non-UV emitting feldspar contaminants were carried out on three OSL samples, yielding three acceptable OSL ages which served (in conjunction with one ^{14}C date) as vital independent age control to validate the $pIRIR_{170}$ ages. The $pIRIR_{170}$ protocol yields ages in substantially better agreement with fading-corrected IR_{50}, quartz-OSL and ^{14}C ages than the $pIRIR_{225}$ and especially the $pIRIR_{290}$ protocols, suggesting the latter signals are insufficiently bleached in this context. The resulting $pIRIR_{170}$ ages are in the correct stratigraphic order, are non-faded and exhibit lower residual doses than the $pIRIR_{225}$. Single aliquot D_e distributions for the $pIRIR_{170}$ tend toward normality irrespective of aliquot size, with few outliers and OD typically ranging from 1.6-30% excluding the very youngest samples (OD 37-87%). The adequacy of bleaching is potentially facies dependent, and it is interesting that the only sample showing clear evidence of partial bleaching (AK8-1) originated from a high-energy deposit in an alluvial fan context. The stability of the CAM D_es across aliquot sizes implies signal averaging masking heterogeneous bleaching is not a serious issue for these samples. Overall it seems that the $pIRIR_{170}$ signal is suitable for dating deposits up to at least MIS4. With this detailed chronology we can begin to consider the Africanders Kloof terrace record in the context of climate driven patterns of aggradation, geomorphic stasis and wetland formation during MIS3.

Acknowledgements

This post-doctoral work is a continuation of the NERC-funded doctoral research project (grant no. 1093015) with additional support from the PAN-KAROO project and the University of Leicester. The authors wish to thank: Prof Andreas Lang, Dr Barbara Mauz and Mrs Susan Packman for input regarding sampling methodology and interpretation of different aspects of the OSL-based results; the two anonymous reviewers for their constructive remarks that helped us to clarify some aspects of the methods and analyses; and Hester and JP Steinberg of Ganora Farm for giving us permission to work on their land. Declarations of interest: none.

References

Adamiec G and Aitken MJ. 1998. Dose-rate conversion factors: update. *Ancient TL* **16**, pp. 37-50

Ainscoe EA, Abdrakhmatov KG, Baikulov S, Carr AS, Elliott AJ, Grűtzner and Walker RT. 2019 ‘Variability in surface rupture between successive earthquakes on the Suusamyr Fault, Kyrgyz Tien Shan: implications for palaeoseismology.’ *Geophysical Journal International* **216**, pp. 703-725.

Aitken MJ. 1985. *Thermoluminescence Dating*, pp. 359, Academic Press, London.

Arnold LJ, Bailey RM and Tucker GE. 2007. ‘Statistical treatment of fluvial dose distributions from southern Colorado arroyo deposits.’ *Quaternary Geochronology* **2** (1-4), pp. 162-167.

Auclair M, Lamothe M and Huot S. 2003. ‘Measurement of anomalous fading for feldspar IRSL using SAR.’ *Radiation Measurements* **37**, pp. 487-497.

Bell WT. 1979. ‘Attenuation factors for the absorbed radiation dose in quartz inclusions for thermoluminescence dating.’ *Ancient TL* **8**, pp. 1-12.

Bhatia MR. 1983. 'Plate tectonics and geochemical composition of sandstone.' *Journal of Geology* **9**: pp. 611-627.

Boardman J. 2014. ‘How old are the gullies (dongas) of the Sneeuberg uplands, Eastern Karoo, South Africa?’ *Catena* **113**, pp. 79-85.

Boardman J, Foster IDL, KM, Favis-Mortlock DT, Mol L, Suich H and Gaynor D. 2017. ‘Long-term studies of land degradation in the Sneeuberg uplands, eastern Karoo, South Africa: A synthesis.’ *Geomorphology* **285**, pp. 106-120.

Boardman J, Holmes PJ, Rhodes EJ and Bateman MD. 2005. ‘Colluvial fan gravels, depositional environments and luminescence dating: A Karoo case study.’ *South African Geographical Journal* **87** (1), pp. 73-79.

Botha GA and Fedoroff N. 1995. ‘Palaeosols in Late Quaternary colluvium, northern KwaZulu-Natal, South Africa. *Journal of African Earth Sciences* **21** (2), pp. 291-311.

Botha GA, Wintle AG and Vogel JC. 1994. ‘Episodic late Quaternary palaeogully erosion in northern KwaZulu-Natal, South Africa.’ *Catena* **23** (3-4), pp. 327-340.

Bousman CB, Partridge PC, Scott L, Metcalfe SE, Vogel JC, Seaman M and Brink JS.1988. ‘Palaeoenvironmental implications of late Pleistocene and Holocene valley fills in Blydefontein Basin, Noupoort, C.P. South Africa.’ *Palaeoecology of Africa* **19**, pp. 43-67.

Braumann SM, Neuhuber S, Fiebig M, Schaefer JM, Hintersberger E, Lűthgens C. 2019. ‘Challenges in constraining ages of fluvial terraces in the Vienna basin (Austria) using combined isochron burial and pIRIR$_{225}$ luminescence dating. *Quaternary International* **509**, pp. 87-102.

Brierley GJ and Fryirs K. 1999. ‘Tributary-trunk stream relations in a cut and fill landscape: a case study from Wolumla catchment, New South Wales, Australia.’ *Geomorphology* **28** (1-2), pp. 61-73.

Buckland CE, Bailey RM and Thomas DSG. 2019. 'Using post-IR IRSL and OSL to date young (< 200 yrs) dryland aeolian dune deposits.' *Radiation Measurements* **126**, pp. 1-12.

Buylaert J-P, Murray AS, Thomsen KJ and Jain M. 2009. 'Testing the potential of an elevated temperature IRSL signal from K-feldspar. *Radiation Measurements* **44**, pp. 560-565.

Buylaert J-P, Jain M, Murray AS, Thomsen KJ, Thiel C and Sohbati R. 2012. 'A robust feldspar luminescence dating methods for Middle and Late Pleistocene sediments. *Boreas* **41**, pp. 435-451.

Buylaert J-P, Thiel C, Murray AS, Vanderberghe D, Yi S and Lu H. 2011. 'IRSL and post-IR IRSL residual doses recorded in modern dust samples from the Chinese Loess Plateau. *Geochronometria* **38**, pp. 432-440.

Buylaert J-P, Murray AS, Gebhardt AC, Sohbati R, Ohlendorf C, Thiel C, Wastegard S, Zolitschka, B. & The PASADO Science Team 2013. Luminescence dating of the PASADO core 5022-1D from Laguna Potrok Aike (Argentina) using IRSL signals from feldspar. *Quaternary Science Reviews* **71**, pp. 70–80.

Carr AS, Hay AS, Powell DM, Livingstone I. 2019. 'Testing post-IR IRSL luminescence dating methods in SW Mojave Desert, California, USA. *Quaternary Geochronology* **49**, pp. 85-91.

Chase BM and Meadows ME. 2007. 'Late Quaternary dynamics of southern Africa's winter rainfall zone.' *Earth Science Reviews* **84** (3-4), 103-138.

Chen Y, Li S and Li B., 2013. 'Residual doses and sensitivity change of post IR IRSL signals from potassium feldspar under different bleaching conditions.' *Geochronometria* **40**, pp. 229–238.

Clarke ML, Vogel JC, Botha GA and Wintle AG. 2003. 'Late Quaternary hillslope evolution recorded in eastern South African colluvial badlands.' *Palaeogeography Palaeoclimatology Palaeoecology* **197** (3-4), pp. 199-212.

Colarossi D, Duller GAT and Roberts HM. 2018. 'Exploring the behaviour of luminescence signals from feldspars: implications for the Single Aliquot Regenerative dose protocol.' *Radiation Measurements* **109**, pp. 35-44.

Colarossi D, Duller GAT, Roberts HM, Tooth S and Lyons R. 2015. 'Comparison of paired quartz and feldspar post-IR IRSL dose distributions in poorly bleached fluvial sediments from South Africa. *Quaternary Geochronology* **30**, pp. 233-238.

Cox, K. G., Macdonald, R and Hornung, G. 1967. Geochemical and petrologic provinces in the Karoo basalts of Southern Africa. *American Mineralogist* **52**, pp. 1451-1474.

Decker JE, Niedermann S and de Wit MJ. 2013. 'Climatically influenced denudation rates of the southern African plateau: Clues to solving a geomorphic paradox. *Geomorphology* **190**, pp. 48–60.

Dietze M, Kreutzer S, Burow C, Fuchs MC, Fischer M and Schmidt C. 2016. 'The abanico plot: Visualising chronometric data with individual standard errors.' *Quaternary Geochronology* **31**, pp. 12-18.

Duller GAT. 2003. 'Distinguishing quartz and feldspar in single grain luminescence measurements.' *Radiation Measurements* **37** (2), pp. 161-165.

Duller GAT and Bøtter-Jensen L. 1993. 'Luminescence from potassium feldspars stimulated by infrared and green light.' *Radiation Protection Dosimetry* **47** (1-4), pp. 683-688.

Fryirs K, Brierley GJ, Preston NJ and Kasai M. 2007. 'Buffers, barriers and blankets: The (dis)connectivity of catchment-scale sediment cascades.' *Catena***70** (1), pp. 49-67.

Fu X and Li SH. 2013. 'A modified multiple-elevated-temperature post-IR IRSL protocol for dating Holocene sediments using K-feldspar.' *Quaternary Geochronology* **17**, pp. 44-54.

Galbraith RF, Roberts RG, Laslett GM, Yoshida H and Olley JM. 1999. 'Optical dating of single and multiple grains of quartz from jinmium rock shelter, northern Australia: Part I, experimental design and statistical models.' *Archaeometry* **41**, pp. 339–364.

Godfrey-Smith DI, Huntley DJ and Chen W-H. 1988. ‘Optical dating studies of quartz and feldspar sediment extracts.’ *Quaternary Science Reviews***1**, pp. 373-380.

Grenfell SE, Grenfell MC, Rowntree KM and Ellery WN. 2014. ‘Fluvial connectivity and climate: A comparison of channel pattern and process in two climatically contrasting fluvial sedimentary systems in South Africa,’ *Geomorphology* **205**, pp. 142-154.

Holmes PJ. 2001. ‘Central Great Karoo headwater catchments and valley fills; an overview of short term change.’ *South African Geographical Journal* **83** (3), pp. 274-282.

Holmes PJ, Boardman J, Parsons AJ and Marker ME.2003. ‘Geomorphological palaeoenvironments of the Sneeuberg Range, Great Karoo, South Africa. *Journal of Quaternary Science* **18** (8), pp. 801-813.

Huntley DJ. 2006. 'An explanation of the power-law decay of luminescence.' *Journal of Physics Condensed Matter* **18** (4), pp. 1359–1365.

Huntley DJ and Baril MR. 1997. ‘The K content of the K-feldspars being measured in optical dating or in thermoluminescence dating. *Ancient TL* **15**, pp. 11-13.

Huntley DJ and Hancock RGV. 2001. ‘The Rb contents of the K-feldspar grains being measured in optical dating.’ *Ancient TL* **19**, pp. 43-46.

Huntley DJ and Lamothe M. 2001. ‘Ubiquity of anomalous fading in K-feldspar and the measurement and corrections for it in optical dating.’ *Canadian Journal of Earth Science* **38**, pp. 1093-1106.

Huntley DJ and Lian OB. 2006. ‘Some observations on tunnelling of trapped electrons in feldspars and their implications for optical dating. *Quaternary Science Reviews* **25**, pp. 2503-2512.

Jain, M., Buylaert, J.P., Thomsen, K.J., Murray, A.S., 2015. Further investigations on “non-fading” in K-Feldspar. *Quaternary International* **362**, 3–7.

Jankoswki NR Jacobs Z and Goldberg P. 2015. 'Optical dating and soil micromorphology at MacCauley's beach, New South Wales, Australia.' *Earth Surface Processes and Landforms* **40**, pp. 229-242.

Kars RH, Reimann T and Wallinga J. 2014. 'Are feldspar SAR protocols appropriate for post-IR IRSL dating? *Quaternary Geochronology* **22**, pp. 126-136.

Keen-Zebert A, Tooth S, Rodnight H, Duller GAT, Roberts HM and Grenfell M. 2013. 'Late Quaternary floodplain reworking and the preservation of alluvial sedimentary archives in unconfined and confined river valleys in the eastern interior of South Africa.' *Geomorphology* **185** (0), pp. 54-66.

Kemp RA. 1985. 'The decalcified Lower Loam at Swanscombe, Kent: a buried Quaternary soil.' *Proceedings of the Geologists' Association* **96**, (4), pp. 343-355.

Kreutzer S, Schmidt C, Fuchs MC, Dietze M, Fisher M and Fuchs, M. 2012. 'Introducing an R package for luminescence dating analysis.' *Ancient TL***30**, pp. 1–7.

Li SH, Sun JM and Zhao H. 2002. 'Optical dating of dune sands in the northeastern deserts of China.' *Palaeogeography, Palaeoclimatology, Palaeoecology***181**, pp. 419-429.

Lowick SE, Trauerstein M and Preusser F. 2012. 'Testing the application of post-IR IRSL dating to fine grain waterlain sediments.' *Quaternary Geochronology* **8**, pp. 33-40.

Lyons R, Tooth S and Duller GA. 2013. 'Chronology and controls of donga (gully) formation in the upper Blood River catchment, KwaZulu-Natal, South Africa: Evidence for a climatic driver of erosion.' *The Holocene* **23** (12), pp. 1875-1887.

Lyons R, Tooth S and Duller GA. 2014. 'Late Quaternary climatic changes revealed by luminescence dating, mineral magnetism and diffuse reflectance spectroscopy of river terrace palaeosols: a new form of geoproxy data for the southern African interior.' *Quaternary Science Reviews* **95**, pp. 43-59.

Marker ME. 1995. ‘Late Quaternary environmental implications from sedimentary sequences at 2 high-altitude Lesotho sites.’ *South African Journal of Science* **91** (6), pp. 294-298.

Medialdea A, Thomsen KJ, Murray AS and Benito G., 2014. ‘Reliability of equivalent-dose determination and age-models in the OSL dating of historical and modern palaeoflood sediments.’ *Quaternary Geochronology,* **22,** pp. 11–24.

Mejdahl V. 1979. ‘Thermoluminescence dating: beta attenuation in quartz grains. *Archaeometry* **21**, pp. 61-73.

Murray AS, Thomsen KJ, Masuda N, Buylaert J-P and Jain M. 2012. ‘Identifying well-bleached quartz using the different bleaching rates of quartz and feldspar luminescence signals. *Radiation Measurements* **47**, pp. 688-695.

Murray AS and Wintle AG. 2000. ‘Luminescence dating of quartz using an improved single-aliquot regenerative-dose protocol.’ *Radiation Measurements* **32** (1), pp. 57-73.

Neudorf CM, Roberts RG and Jacobs Z. 2012. ‘Sources of overdispersion in a K-rich feldspar sample from north-central India: Insights from D_e, *K* content and IRSL age distributions for individual grains.’ *Radiation Measurements* **47**, pp. 696-702.

Neumann ER, Svensen H, Galerne CY and Planck S*.* 2011. ‘Multistage evolution of dolerites in the Karoo large igneous province, central South Africa. *Journal of Petrology* **52** (5), pp. 959-984.

Nian X, Bailey RM and Zhou L. 2012. ‘Investigations of the post-IR IRSL protocol applied to single K-feldspar grains from fluvial sediment samples.’ *Radiation Measurements* **47**, pp. 703-709.

Oghenekome ME. 2012. 'Sedimentary environments and provenance of the Balfour Formation (Beaufort Group) in the area between Bedford and Adelaide, Eastern Cape Province, South Africa. MSc thesis, University of Forte Hare, Alice, South Africa.

Oldknow CJ. 2016. Late Quaternary landscape evolution in the Great Karoo, South Africa: Processes and drivers. PhD thesis, University of Liverpool, Liverpool, UK.

Oldknow CJ and Hooke JM. 2017. ‘Alluvial terrace development and changing landscape connectivity in the Great Karoo, South Africa. Insights from the Wilgerbosch River catchment, Sneeuberg. *Geomorphology* **288**, pp. 12-38.

Olley JM, Pietsch T and Roberts RG. 2004. ‘Optical dating of Holocene sediments from a variety of geomorphic settings using single grains of quartz. *Geomorphology* **60**, pp. 337-358.

Prescott JR and Hutton JT. 1994. ‘Cosmic ray contributions to dose rates for luminescence and ESR dating: large depths and long term variations.’ *Radiation Measurements* **23**, pp. 497-500.

Ramluckan VR. 1992. The petrology and geochemistry of the Karoo sequence basaltic rocks in the Natal Drakensberg at Sani Pass. MSc thesis. University of Durban-Westville, South Africa.

Reimann T and Tsukamoto S. 2012. 'Dating the recent past (< 500 years) by post-IR IRSL feldspar - Examples from the North Sea and Baltic Sea coast.' *Quaternary Geochronology* **10** (10), pp. 180-187.

Reimann T, Tsukamoto S, Naumann M and Frechen M. 2011. ‘The potential using K-rich feldspars for optical dating of young coastal sediments – A test case from Darss-Zingst peninsula (southern Baltic Sea coast).’ *Quaternary Geochronology* **6** (2), pp. 207-222.

Rhodes E. 2015. ‘Dating sediments using potassium feldspar single-grain IRSL: initial methodological considerations.’ *Quaternary International* **362**, pp. 14-22.

Roberts HM. 2012. ‘Testing Post-IR IRSL protocols for minimising fading in feldspars, using Alaskan loess with independent chronological control.’ *Radiation Measurements.***47**, pp. 716–724.

Rodnight H, Duller GAT, Wintle AG and Tooth S. 2006. ‘Assessing the reproducibility and accuracy of optical dating of fluvial deposits.’ *Quaternary Geochronology* **1** (2), pp. 109-120.

Rowell ALK, Thomas DSG, Bailey KM and Holmes PJ. 2018. ‘Sand ramps as palaeoenvironmental archives: integrating general principles and regional contexts through reanalysis of the Klipkraal sands, South Africa. *Geomorphology* **311**, pp. 103-113.

Schultz BR. 1980. *Climate of South Africa, Part 9, General Survey.* Weather Bureau, Department of Transport, Pretoria.

Shen Z, Mauz B, Lang A, Bloemendal J and Dearing J. 2007. 'Optical dating of Holocene lake sediments: Elimination of the feldspar component in fine silt quartz samples.' *Quaternary Geochronology* **2** (1-4), pp. 150-154.

Smedley RK, Buylaert J-P and Újvári G. 2019. 'Comparing the accuracy and precision of luminescence ages for partially-bleached sediments using single grains of K-feldspar and quartz, *Quaternary Geochronology* 53, 101007

Sohbati, R., Murray, A. S., Buylaert, J.-P., Ortuño, M., Cunha, P. P. & Masana, E. 2012 (April): 'Luminescence dating of Pleistocene alluvial sediments affected by the Alhama de Murcia fault (eastern Betics, Spain) – a comparison between OSL, IRSL and post-IR IRSL ages.' *Boreas* **41**, pp. 250–262.

Sugden JM. 1989. *Palaeoecology of the central and marginal uplands of the Karoo, South Africa.* University of Cape Town, Cape Town, pp. 384.

Temme A, Baartman JEM, Botha GA,Veldkamp A, Jongmans AG and Wallinga J.2008. 'Climatic controls on late Pleistocene landscape evolution of the Okhombe valley, KwaZulu-Natal, South Africa.' *Geomorphology* **99** (1-4), pp. 280-295.

Thiel C, Buylaert J.-P, Murray A, Terhorst B, Hofer I, Tsukamoto S and Frechen M. 2011. 'Luminescence dating of the Stratzing loess profile (Austria) - testing the potential of an elevated temperature post-IR IRSL protocol.' *Quaternary International***234**, pp. 23–31.

Thomsen KJ, Murray AS, Jain M, Bøtter-Jensen L. 2008. 'Laboratory fading rates of various luminescence signals from feldspar-rich sediment extracts. *Radiation Measurements* **43**, pp. 1474-1486.

Trauerstein M, Lowick SE, Preusser F, Schlunegger F. 2014. 'Small aliquot and single grain IRSL and post-IR IRSL dating of fluvial and alluvial sediments from the Pativilca Valley, Peru.' *Quaternary Geochronology* **22**, pp. 163-174.

Turner BR. 1978. Sedimentary patterns of uranium mineralisation in the Beaufort Group of the southern Karoo (Gondwana) Basin, South Africa. In: Miall AD. (Ed.). *Fluvial Sedimentology, Canadian Association of Petroleum Geologists,* Memoir **5**, pp. 831-848.

Vermeesch P. 2009. 'RadialPlotter: a Java application for fission track, luminescence and other radial plots.' *Radiation Measurements* **44**, pp. 409-410.

Wintle, AG, Li SH, Botha GA. 1993. Luminescence dating of colluvial deposits from Natal, South Africa. S. Afr. J. Sci. 89, 77-82.

Wintle, AG, Botha GA, Li SH, Vogel, JC. 1995a. A chronological framework for colluviation during the last 110kyr in KwaZulu/Natal. *South African Journal of Science* **91**, pp. 134-139.

Wintle, AG, Li SH, Botha, GA, Vogel, JC. 1995b. Evaluation of luminescence dating procedures applied to late-Holocene colluvium near St Paul's Mission, Natal, South Africa. *The Holocene* **5**, pp. 97-102.

Wright VP. 1990. 'Estimating rates of calcrete formation and sediment accretion in ancient alluvial deposits.' *Geological Magazine* **127** (3), pp. 273-276.

Wright VP, Platt NH, Marriott SB and Beck VH. 1995. 'A classification of rhizogenic (root-formed) calcretes, with examples from the Upper Jurassic-Lower Cretaecous of Spain and Upper Cretaceous of southern France.' *Sedimentary Geology* **100** (1-4), pp. 143-158.

Yi S, Buylaert J-P, Murray AS, Lu H, Thiel C and Zeng L. 2016. 'A detailed post-IR IRSL dating study of the Niuyangzigou loess site in north-east China.' *Boreas* **45**, pp. 644-657.

Zanders A and Hilgers A. 2013. Potential and limits of OSL, TT-OSL, IRSL and $pIRIR_{290}$ dating methods applied on a Middle Pleistocene sediment records of Lake El'gygytyn, Russia. *Climate of the Past* **9**, pp. 719-733.

Supplementary Information

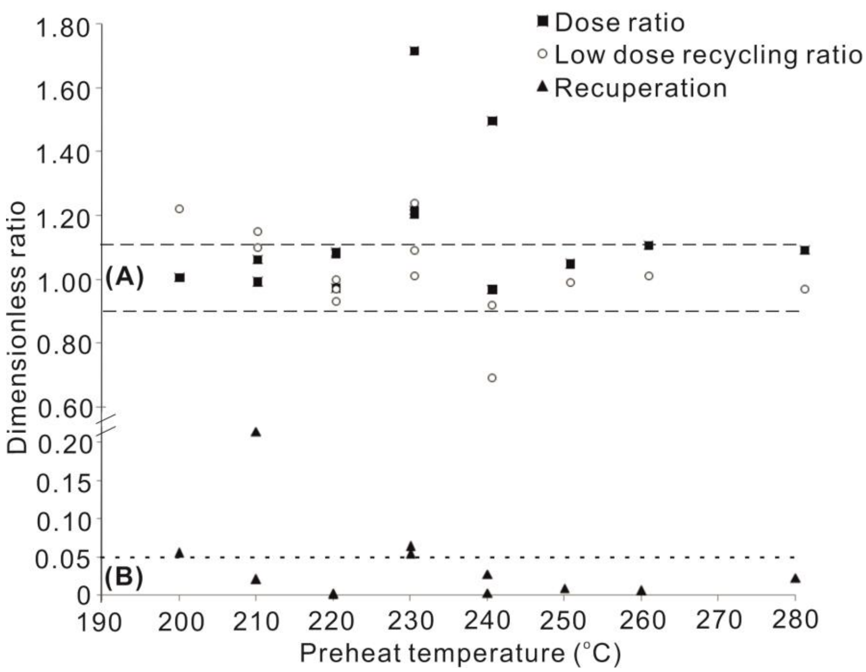

Fig. S1. Preheat/dose recovery test results for quartz sample AK8-1. Administered dose was 43.6 Gy. Shown are: (a) M/G dose ratio and low dose (8.7 Gy) recycling points that fall within ±10% of unity; and (b) recuperation values less than 0.05 (5%).

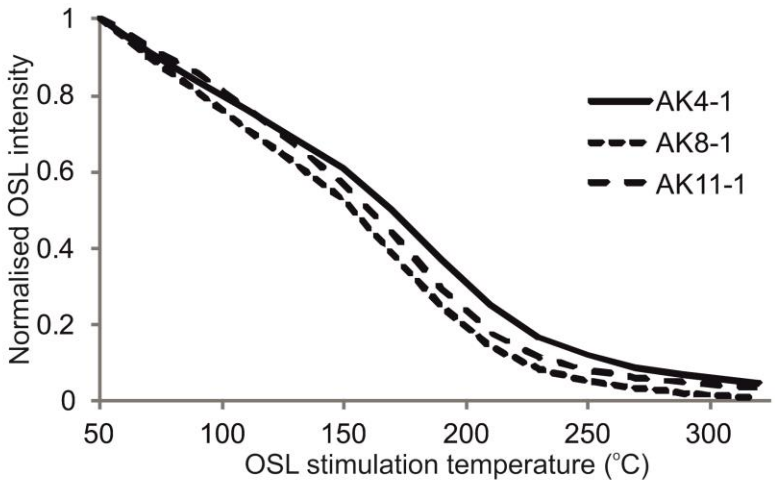

Fig. S2. OSL intensity plotted versus stimulation temperatures (normalized to the 50 ºC OSL intensity).

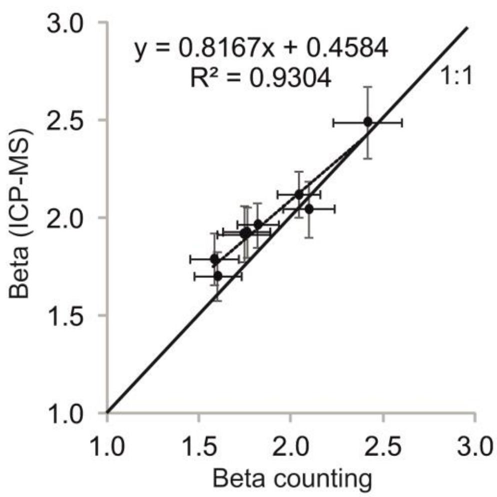

Fig. S3. Comparison of beta dose rates obtained using GM beta counting (x) and ICP-MS (y). Note overlap of datapoints (within 1σ error) with 1:1 line.

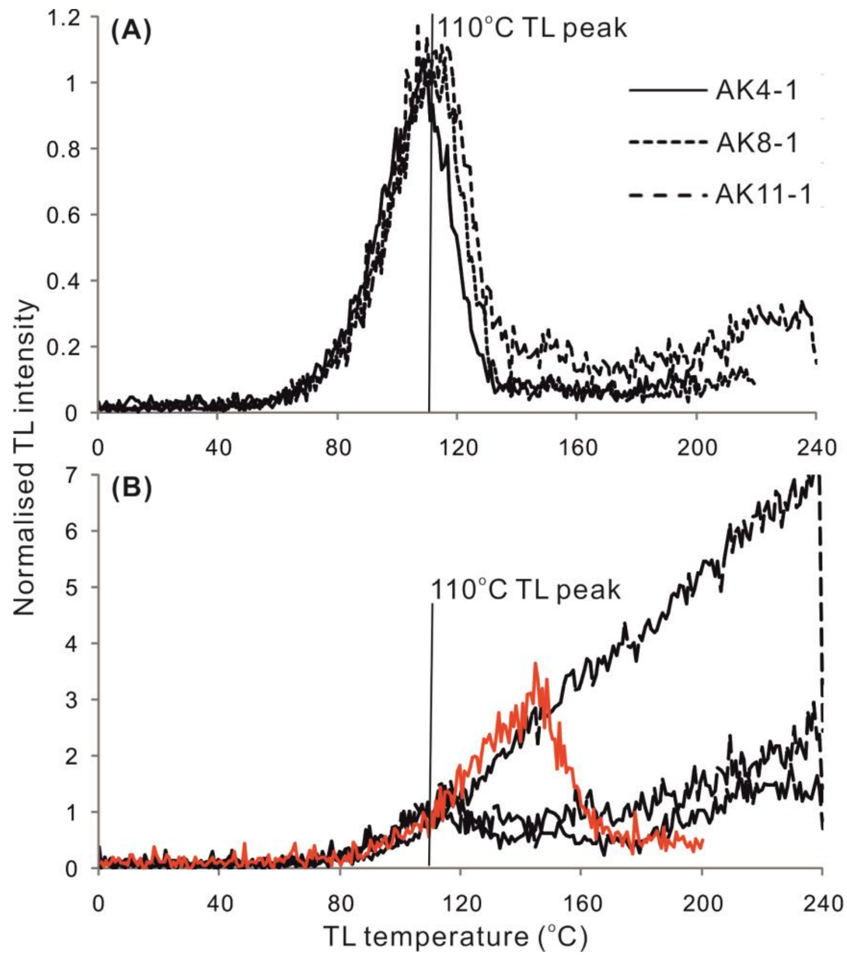

Fig. S4. Thermoluminescence (TL) curves normalized to the 110 ºC peak: (A) Representative TL curves obtained for AK4-1, AK8-1 and AK11-1 which show a clear 110 ºC peak indicative of quartz; (B) Examples of aliquots from both AK4-1 (red line) and AK11-1 which yielded TL behaviour that is contrary to that expected for pure quartz.

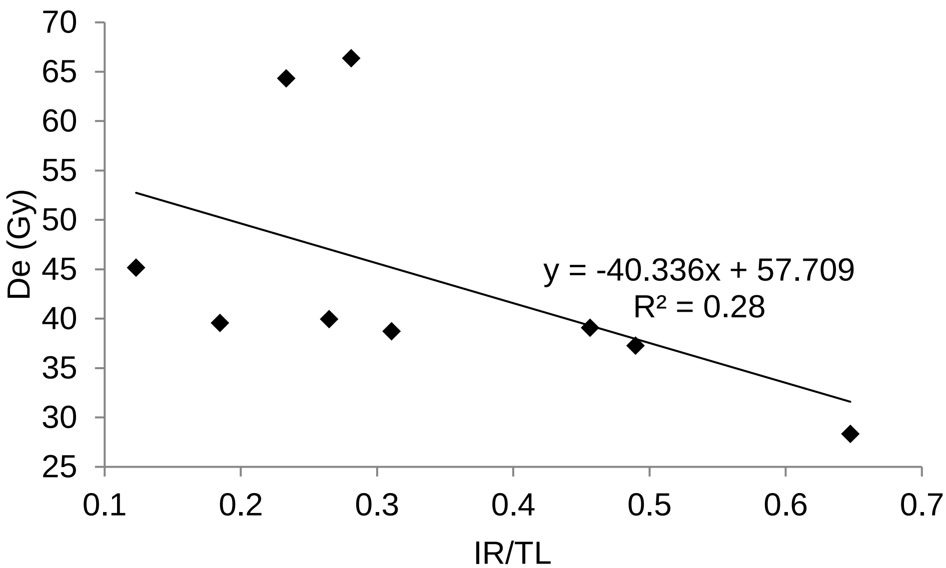

Fig. S5. The D_e plotted as a function of the IR/TL ratio for aliquots from sample AK11-1 exhibiting a 110 ºC TL peak which is part of the ascending limb of higher temperature (feldspar) TL peaks.

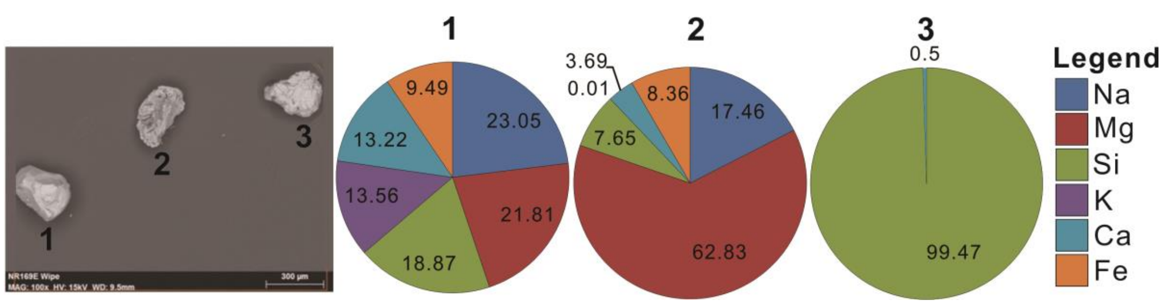

Fig. S6. Results of combined SEM/XRF analyses on three etched grains from AK11-1.

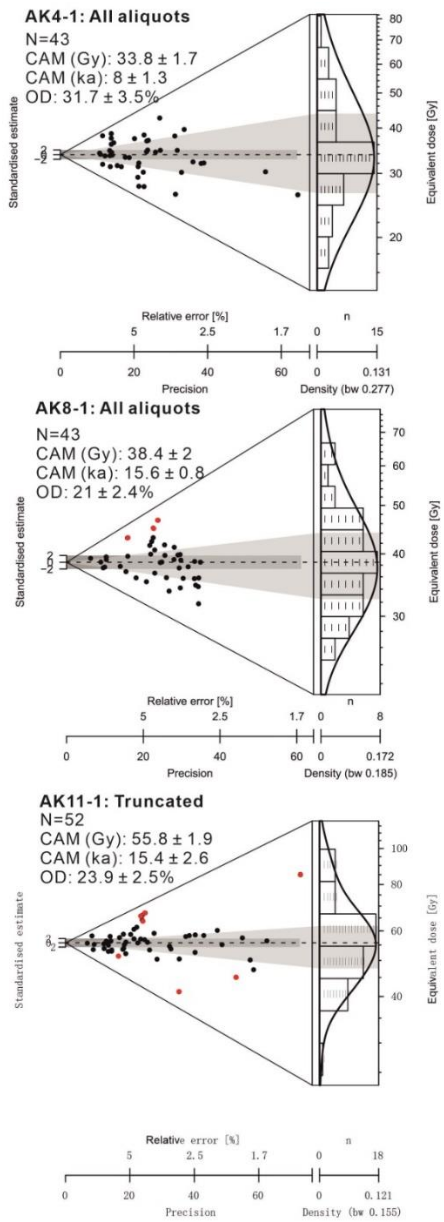

Fig. S7. Abanico plots for OSL D_e data. Statistical outliers are highlighted in red and were removed following Medialdea et al. (2014).

Table S1 Dose rate data.Beta and gamma dose rates were derived from ICP-MS measurements of sample tube ends corrected for grain size following Mejdahl (1979) and Redhead (2002) and water content following Aitken (1985) using element conversion factors of Guerin et al. (2011).U, Th and K contents determined using ICP-MS with relative uncertainties of 10% (U and Th) and 5% (K).Cosmic dose rates follow Prescott and Hutton (1994).

Sample	**U (ppm)**	**Th (ppm)**	**K (%)**	**Grain size (μm)**	**Int. beta dose rate (Gy ka^{-1})**	**Ext. beta dose rate (Gy ka^{-1})**	**Gamma dose rate (Gy ka^{-1})**	**Cosmic dose rate (Gy ka^{-1})**	**Total dose rate (Gy ka^{-1})**
AK4-1	2.6	14.5	2.5	90-300	0.78 ± 0.37	2.22 ± 0.18	1.57 ± 0.10	0.22 ± 0.01	4.79 ± 0.42
AK8-1	1.3	9.0	1.6	200-300	0.98 ± 0.19	1.28 ± 0.10	0.91 ± 0.06	0.21 ± 0.01	3.37 ± 0.22
AK8-2	1.7	12.2	2.2	200-300	0.98 ± 0.19	1.77 ± 0.14	1.25 ± 0.08	0.17 ± 0.01	4.17 ± 0.25
AK11-1	1.8	13.3	2.3	200-300	0.98 ± 0.19	1.93 ± 0.15	1.37 ± 0.09	0.18 ± 0.01	4.45 ± 0.26
AK11-2	2.3	14.5	2.6	180-250	0.86 ± 0.13	2.21 ± 0.17	1.56 ± 0.10	0.24 ± 0.01	4.86 ± 0.24
AK11-3	2.1	13.1	2.3	180-250	0.86 ± 0.13	1.89 ± 0.14	1.35 ± 0.09	0.20 ± 0.01	4.30 ± 0.21
AK11-4	2.5	11.5	1.9	212-250	0.92 ± 0.08	1.74 ± 0.13	1.28 ± 0.08	0.19 ± 0.01	4.12 ± 0.17
AK12-1	1.2	7.6	1.6	180-250	0.86 ± 0.13	1.28 ± 0.10	0.86 ± 0.06	0.26 ± 0.01	3.26 ± 0.17
AK12-2	1.9	11.2	2.1	212-250	0.92 ± 0.08	1.80 ± 0.14	1.25 ± 0.08	0.26 ± 0.01	4.23 ± 0.18
AK12-3	2.4	12.1	2.2	212-250	0.92 ± 0.08	1.90 ± 0.14	1.36 ± 0.09	0.24 ± 0.01	4.42 ± 0.19
AK12-4	2.4	13.4	2.3	180-212	0.79 ± 0.07	2.00 ± 0.15	1.43 ± 0.10	0.23 ± 0.01	4.45 ± 0.19
AK12-5	2.5	14.5	2.7	180-250	0.86 ± 0.13	2.29 ± 0.17	1.60 ± 0.11	0.22 ± 0.01	4.97 ± 0.24
AK12-6	3.6	14.5	2.1	212-250	0.92 ± 0.08	1.85 ± 0.13	1.45 ± 0.10	0.20 ± 0.01	4.43 ± 0.18
AK12-7	2.4	15.1	2.8	212-250	0.92 ± 0.08	2.02 ± 0.15	1.43 ± 0.09	0.20 ± 0.01	4.57 ± 0.19
AK12-8	2.6	12.2	2.1	212-250	0.92 ± 0.08	1.79 ± 0.13	1.31 ± 0.09	0.19 ± 0.01	4.21 ± 0.18
AK12-9	2.9	12.5	2.2	212-250	0.92 ± 0.08	1.97 ± 0.14	1.43 ± 0.09	0.17 ± 0.01	4.48 ± 0.19
AK13-1	2.8	11.8	2.1	212-250	0.86 ± 0.13	1.90 ± 0.14	1.36 ± 0.09	0.26 ± 0.01	4.38 ± 0.21
AK13-2	2.6	12.0	2.0	212-250	0.92 ± 0.08	1.81 ± 0.13	1.32 ± 0.09	0.22 ± 0.01	4.27 ± 0.18
AK15-1	2.8	15.8	3.0	212-250	0.92 ± 0.08	2.35 ± 0.17	1.64 ± 0.11	0.26 ± 0.01	5.17 ± 0.22

Final version published in Quaternary Geochronology available here:
https://www.sciencedirect.com/science/article/pii/S1871101420300133

Table S2

SAR protocols used for quartz OSL and feldspar post-IR IRSL.

	a) Quartz OSL		b) Feldspar post-IR IRSL	
Step	Treatment	Measured	Treatment	Measured
1	Dose	-	Dose	-
2	Preheat (220 ˚C for 10 s)	-	Preheat (200 ˚C for 60 s)	-
3	OSL (125 ˚C for 40 s)	Lx	IRSL (50 ˚C for 100 s)	-
4	Test dose (~4 Gy)	-	IRSL (170 ˚C for 300 s)	Lx
5	Cutheat (200 ˚C for 0 s)	-	Test dose (~30% D_e)	-
6	OSL (125 ˚C for 40 s)	Tx	Preheat (200 ˚C for 60 s)	-
7	Return to step 1		IRSL (50 ˚C for 100 s)	-
8			IRSL (170 ˚C for 300 s)	Tx
9			IRSL (220 ˚C for 300 s)	-
10			Return to step 1	

Table S3

Modified SAR protocol used to determine the thermal behaviour of the OSL signal. *OSL temperature was increased in 20 ^{o}C increments for each cycle (L_x) beginning at 50 ^{o}C, ending at 325 ^{o}C.

	a) Quartz OSL	
Step	Treatment	Measured
1	Dose	-
2	Preheat (220 ˚C for 10 s)	-
3	***OSL (50-325 ˚C for 40 s)**	Lx
4	Test dose (~4 Gy)	-
5	Cutheat (200 ˚C for 0 s)	-
6	OSL (125 ˚C for 40 s)	Tx
7	Return to step 1	

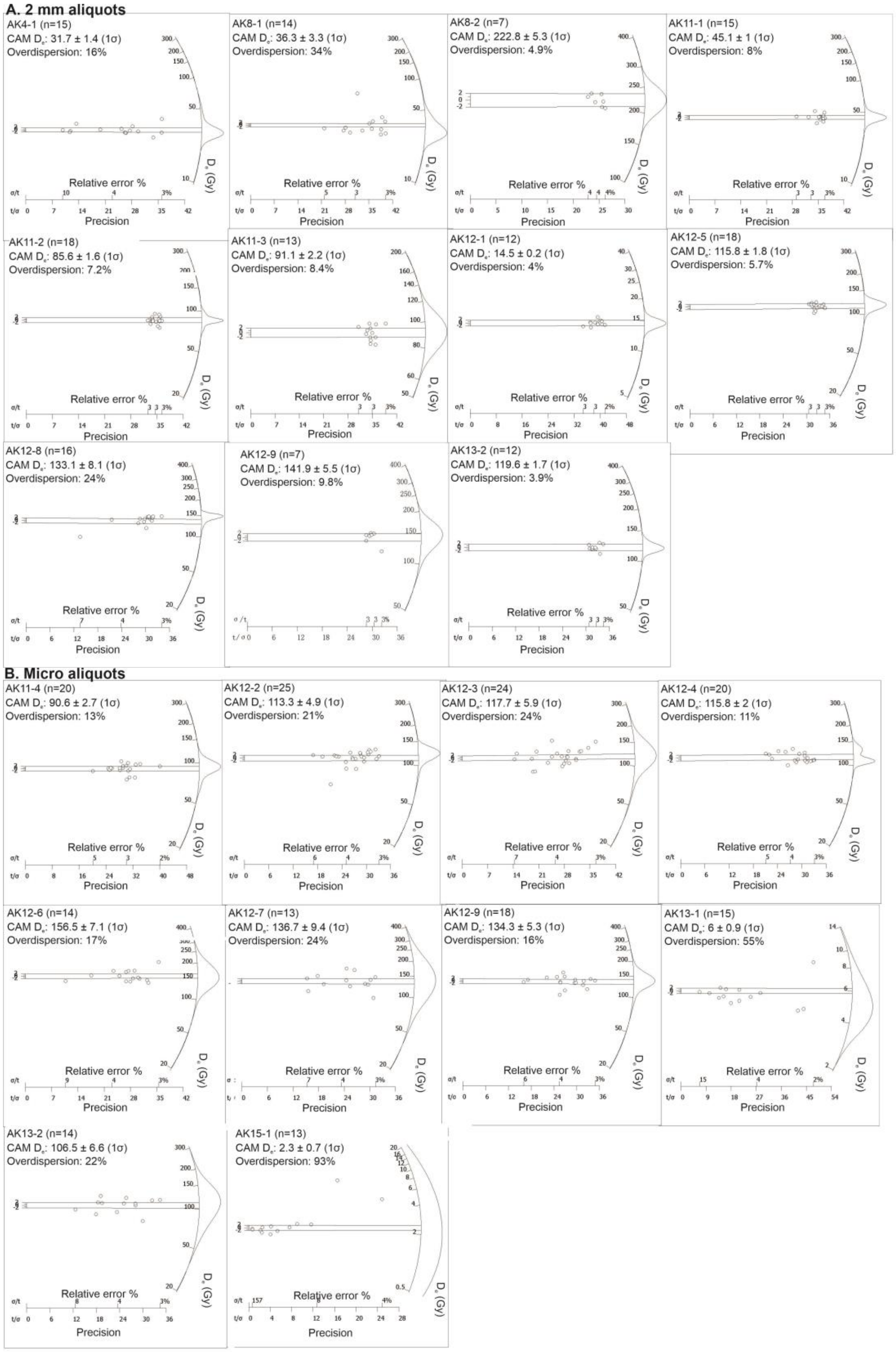

Fig. S8. Radial plots showing D_e values determined using the IR_{50} protocol applied to: A. 2 mm aliquots; and B. Micro-aliquots.

Table S4.

Internal checks of IR_{50} performance conducted on 2 mm aliquots. *Refers to IR_{50} measurements prior to $pIRIR_{225}$ given for comparative purposes.

Sample	DRR Natural Light	DRR Added dose	g-value (% per decade)	Residual dose (Gy).
AK4-1	-	-	2.48 ± 0.52	-
AK8-1	0.96 ± 0.01	-	2.15 ± 0.59	0.33 ± 0.04
AK8-2	-	-	1.84 ± 0.71	0.89 ± 0.29
AK11-1	-	-	4.95 ± 0.51	-
AK11-2	0.97 ± 0	-	2.25 ± 0.52	0.41 ± 0.05
AK11-3	1.01 ± 0.01	-	2.59 ± 0.60	0.51 ± 0.07 *1.45 ± 0.27
AK11-4	-	-	-	-
AK12-1	0.97 ± 0	-	2.98 ± 0.29	-
AK12-2	1.01 ± 0.02	-	1.81 ± 0.28	-
AK12-3	-	0.98 ± 0.03	2.05 ± 0.25	0.97 ± 0.14
AK12-4	-	0.89 ± 0.04	2.18 ± 0.17	-
AK12-5	0.97 ± 0	-	2.66 ± 0.18	0.59 ± 0.16 *2.39 ± 0.29
AK12-6	-	-	-	-
AK12-7	-	0.96 ± 0.09	3.09 ± 0.38	0.98 ± 0.16 *3.56 ± 2.08
AK12-8	1.01 ± 0	0.91 ± 0.04	1.97 ± 0.17	1.85 ± 0
AK12-9	-	**1.06 ± 0.02	1.79 ± 0.41	-
WGK4-1	0.96 ± 0.01	-	2.88 ± 0.43	0.47 ± 0.04
AK12-X	0.96 ± 0.01	-	2.13 ± 0.25	-
Average	**0.98 ± 0.02**	**0.93 ± 0.04**	**2.49 ± 0.67**	**0.76 ± 0.57**

Table S5.

Results of IR_{50} measurements for 2 mm aliquots (top) and small aliquots (bottom). Shown are the number of aliquots measured over the number passing the rejection criteria (n/n), the observed OD, the CAM D_e and resulting CAM ages (ka).

Small aliquots 2 mm					
Sample	n/n	OD%	CAM D_e (Gy)	Age (ka)	Fading corrected age (ka)
AK4-1	15/16	16.0	31.7 ± 1.4	6.6 ± 0.5	8.3 ± 0.6
AK8-1	14/14	34.0	36.3 ± 3.3	10.8 ± 1	13.6 ± 1.3
AK8-2	7/7	4.9	222.8 ± 5.3	53.9 ± 1.3	-
AK11-1	14/15	6.4	45.1 ± 1	10.1 ± 0.3	12.7 ± 0.4
AK11-2	18/18	4.9	85.6 ± 1.6	17.6 ± 0.4	22.4 ± 0.6
AK11-3	13/13	8.4	91.1 ± 2.2	21.2 ± 0.6	27.0 ± 0.9
AK12-1	12/12	4.0	14.5 ± 0.2	4.4 ± 0.2	5.5 ± 0.3
AK12-5	18/18	5.0	115.8 ± 1.8	26.0 ± 0.4	-
AK12-8	13/16	1.6	133.1 ± 8.1	29.9 ± 1.9	-
AK12-9	7/7	9.6	141.9 ± 5.5	31.7 ± 1.4	-
AK13-2	12/12	3.6	119.6 ± 1.7	28.0 ± 1.7	-

Micro-aliquots					
Sample	n/n	OD%	CAM D_e (Gy)	Age (ka)	Fading corrected age (ka)
AK11-4	20/22	13	90.6 ± 2.7	22 ± 0.7	-
AK12-2	25/28	21	113.3 ± 4.9	26.8 ± 1.2	-
AK12-3	24/24	24	117.7 ± 5.9	26.6 ± 1.4	-
AK12-4	20/22	11	115.8 ± 3	26.0 ± 0.7	-
AK12-6	14/15	17	156.5 ± 7.1	35.0 ± 1.6	-
AK12-7	13/13	24	136.7 ± 9.4	30.7 ± 2.1	-
AK12-9	18/18	16	134.3 ± 5.3	30.2 ± 1.3	-
AK13-1	15/18	55	6.0 ± 0.9	1.4 ± 0.3	1.7 ± 0.4
AK13-2	14/16	22	106.5 ± 6.6	24.9 ± 1.6	-
AK15-1	13/17	93	2.3 ± 0.7	0.5 ± 0.3	0.6 ± 0.3

Final version published in Quaternary Geochronology available here:
https://www.sciencedirect.com/science/article/pii/S1871101420300133

Table S6.

Comparison of skew, kurtosis and OD for pIRIR$_{170}$ D_e distributions obtained using small (top) and micro-aliquots (bottom).

2 mm aliquots	Before outlier removal			After outlier removal		
Sample	Skew	Kurtosis	OD%	Skew	Kurtosis	OD %
AK4-1	-1.68	3.24	17.0	-0.71	-0.39	7.3
AK8-1	2.88	8.75	30.0	-0.49	-0.97	7.8
AK8-2	0.66	-1.51	11.0	1.22	0.65	9.3
AK11-1	0.40	-0.48	6.4	-	-	-
AK11-2	-0.04	-0.10	4.9	0.16	-1.25	1.2
AK11-3	-0.20	-0.45	7.5	-	-	-
AK12-1	0.49	0.95	4.0	-	-	-
AK12-5	-0.51	0.07	4.6	-	-	-
AK12-8	0.90	3.60	9.6	-	-	-

Micro-aliquots	Before outlier removal			After outlier removal		
Sample	Skew	Kurtosis	OD%	Skew	Kurtosis	OD %
AK11-4	-1.67	4.23	29	-0.25	-0.89	09.7
AK12-2	0.83	3.60	28	-0.2	-1.20	14.0
AK12-3	1.60	6.93	21	-0.15	-0.34	09.3
AK12-4	1.30	1.69	23	-0.36	-0.91	15.0
AK12-6	0.57	-0.34	21	0.22	-0.18	17.0
AK12-7	0.39	1.31	14	-0.85	0.82	06.9
AK12-9	0.01	-0.26	18	-	-	-
AK13-1	3.26	11.32	37	0.63	-0.61	14.0
AK13-2	0.82	2.14	29	0.40	0.53	11.0
AK15-1	2.69	7.42	87	0.31	-1.52	46.0

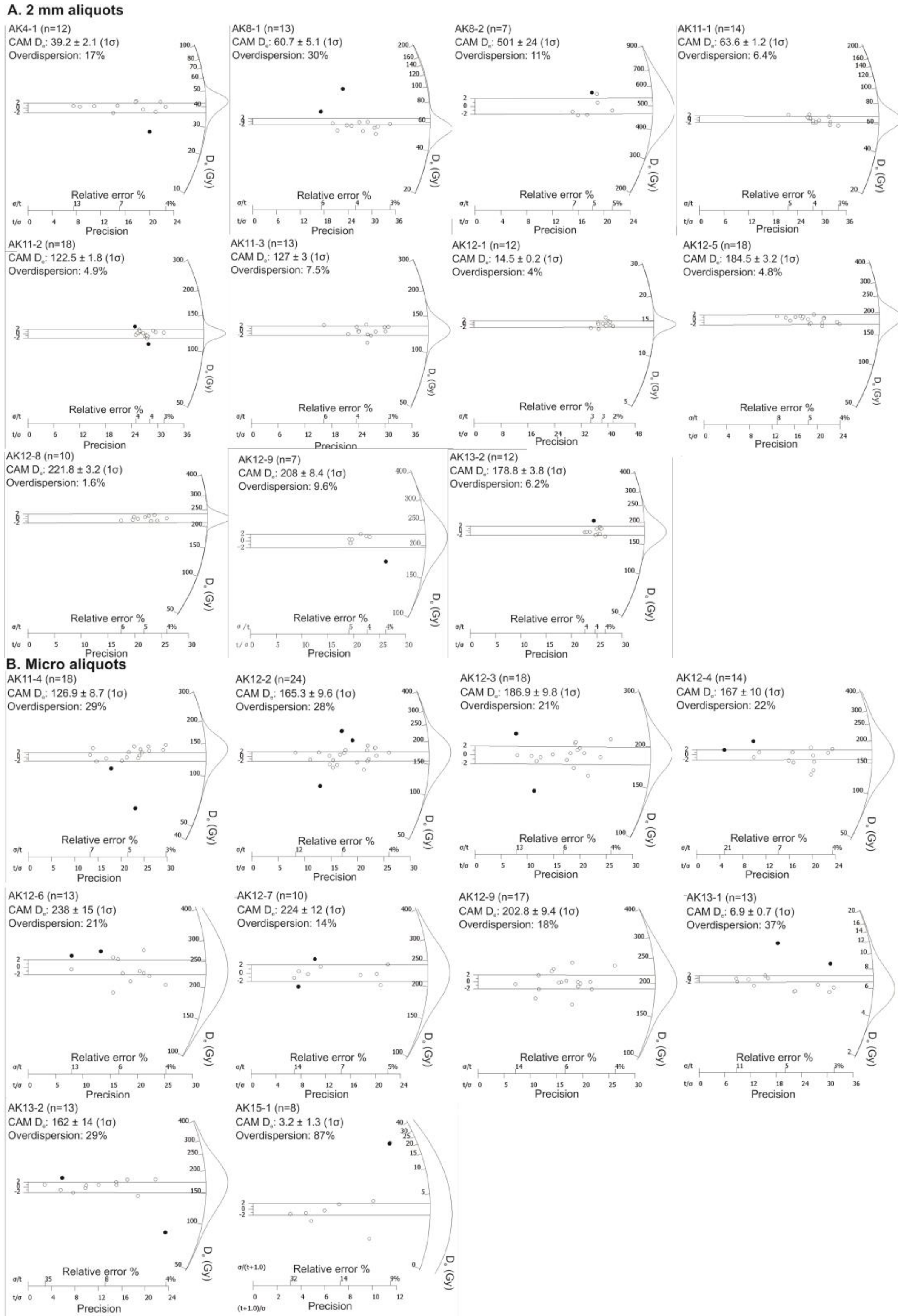

Fig. S9. Radial plots showing D_e values determined using the $pIRIR_{170}$ protocol applied to: A. 2 mm aliquots; and B. micro-aliquots. Note: (i) Solid black dots represent statistical outliers which are omitted in the final ages reported (Table 4, Fig. 10); (ii) AK12-9 micro-aliquot $pIRIR_{170}$ age is used in the chronology (Fig. 10).

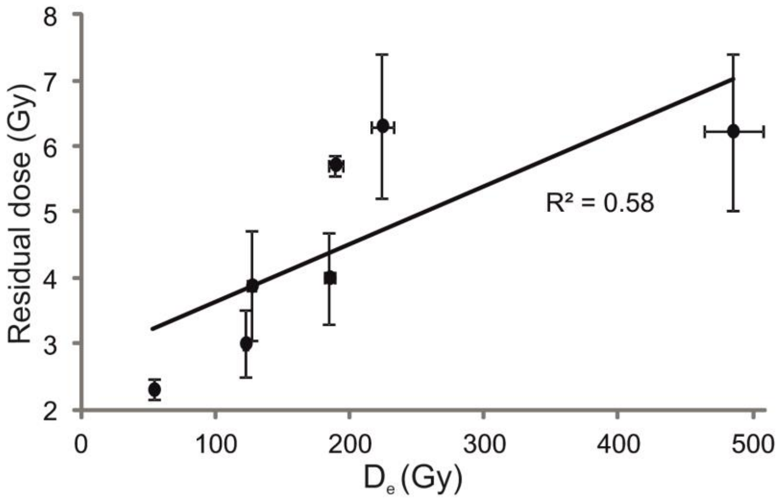

Fig. S10. Dependency of the residual dose on sample D_e. Note: AK12-8 with a residual dose of 20 Gy is omitted from the analysis for reasons outlined in the main text.